Available online at www.sciencedirect.com
ScienceDirect
Geochimica et Cosmochimica Acta 71 (2007) 5135–5154
Geochimica et Cosmochimica Acta
www.elsevier.com/locate/gca

Bubble-induced porewater mixing: A 3-D model for deep porewater irrigation

Matthias Haeckel [a,b,*], Bernard P. Boudreau [a], Klaus Wallmann [b]

[a] Dalhousie University, Department of Oceanography, 1355 Oxford Street, Halifax, NS, Canada B3H 4J1
[b] Leibniz Institute for Marine Sciences (IFM-GEOMAR), Wischhofstr. 1-3, D-24148 Kiel, Germany

Received 21 September 2006; accepted in revised form 17 August 2007; available online 14 September 2007

Abstract

Porewater data from vent sites of the northeastern shelf off Sakhalin Island, Sea of Okhotsk, exhibit bottom-water concentrations down to a sediment depth of up to 300 cm. Below this depth, solute concentrations rapidly change due to methanogenesis and anaerobic methane oxidation (AMO). The profile shapes suggest an irrigation-like process that mixes on a meter scale. At these sites active gas emanation into the overlying water column and near-surface gas hydrates are commonly observed. We propose that methane gas bubbles rise through the soft surface sediments and cause mixing of the porewater.

Mathematically, the bubble-induced irrigation can be described by eddy diffusion enhancing the diffusive transport of solutes by several orders of magnitude. A 3-D numerical transport-reaction model was developed to investigate the parameters defining the mixing process, such as bubble rise velocity, tube size, tube distribution in the sediment, and ebullition frequency.

Model consistency with the field data requires eddy diffusivities $\geqslant 1 \times 10^5$ cm^2/a, tube densities of >4 tubes/m^2 (equivalent to a tube spacing of <40 cm), active gas seepage for more than a few weeks or months, and moderate to low diagenetic reaction rates of solutes. The corresponding methane gas fluxes that are predicted from the results of the model realizations range from 1×10^3–5×10^5 L/(m^2 a). Due to bubble mixing, solute fluxes in these sediments are increased by a factor of 3 and the maximum AMO rate by a factor of 7.

1. INTRODUCTION

The ebullition of methane gas from sediments and soils into overlying waters and ultimately into the atmosphere has been recognized as an important transport process in the global carbon cycle. The largest source to the atmosphere comes from wetlands ranging from 115 to 237 Tg of CH_4 per year (IPCC, 2001). Estimates of annual methane emissions from marine sources, such as seeps and mud volcanoes, are an order of magnitude lower, ranging from 5 to 33 Tg (Dimitrov, 2002; Judd et al., 2002; Dimitrov, 2003; Judd, 2003; Milkov et al., 2003; Milkov and Etiope, 2005; Wallmann et al., 2006b). Though most of the methane flux, especially from the deep water, is oxidized at the seafloor and in the water column, about 6 Tg/a of CH_4 is estimated to reach the atmosphere (Milkov et al., 2003) and thus, may have an impact on global climate change. Gas bubbles also seem to get stripped of methane while rising to the sea surface, exchanging CH_4 for nitrogen and oxygen (McGinnis et al., 2006). However, other studies show that methane gas bubbles from deep water can reach the atmosphere if coated with oil (MacDonald et al., 2002) or a gas hydrate skin (Sauter et al., 2006).

Gas bubbles rising through surface sediments have been widely observed and investigated in coastal sediments (e.g., Reeburgh, 1969; Martens, 1976; Martens and Klump, 1980; Chanton et al., 1989; Anderson et al., 1998; Martens et al., 1998). In these sediments, apparent diffusivities 2–3 times higher than molecular diffusion have been determined for dissolved constituents. This was attributed to gas bubble

* Corresponding author. Present address: Leibniz Institute for Marine Sciences (IFM-GEOMAR), Wischhofstr. 1-3, D-24148 Kiel, Germany. Fax: +49 431 6002928.
E-mail address: mhaeckel@ifm-geomar.de (M. Haeckel).

0016-7037/$ - see front matter © 2007 Elsevier Ltd. All rights reserved.
doi:10.1016/j.gca.2007.08.011

tubes that stay open and hence, facilitate the exchange of porewater and bottom-water (Martens, 1976; Martens et al., 1980; Martens and Klump, 1980; Kipphut and Martens, 1982).

Porewater profiles with a bottom-water signature, present in sediment to depths of several meters, have repeatedly been reported in the literature (e.g., Schulz et al., 1994; Niewöhner et al., 1998). Commonly, these profiles have been explained by meter-scale bioirrigation of unknown macrofauna, but Fossing et al. (2000) also mention the possibility of methane ebullition. In the respective studies, these types of porewater distributions are found in organic-rich sediments at continental margins and other high-productivity areas, such as the Congo Fan and the Amazon Shelf, as well as in upwelling regions, such as the South Atlantic off Namibia. In this study, we report the observation of similar porewater profiles in the organic-rich sediments northeast off Sakhalin Island in the Sea of Okhotsk. Here, the bottom-water signature of the porewater reaches down as far as 3 m into the sediment.

While bioirrigation has been shown to occur in the top few decimetres of the sediment (e.g., Aller, 1980; Aller and Aller, 1992; Schlüter et al., 2000; Meile et al., 2001), we propose that irrigation caused by rising gas bubbles is more likely to explain such observations on a meter scale. Methane gas bubbles produced by methanogenesis or methane hydrate dissociation rise through the sediment, thereby, mixing the porewater and ultimately mixing bottom-water concentrations down into the sediment. The wake of a rising gas bubble leads to turbulent mixing of porewater. An eddy diffusion constant, K_{eddy}, can be assigned to this process. We show that eddy diffusivities for this mixing process can be several orders of magnitude larger than molecular diffusion.

In this paper, we present a model investigation of the diffusive mixing of porewater constituents engendered by gas bubbles rising through surface sediments. First, we analyse porewater data from vent sites located in an area called 'Obzhirov Flare', northeast off Sakhalin Island, Sea of Okhotsk, using a 1-D transport-reaction model. Then, we develop a transient 3-D numerical transport-reaction model to simulate the mixing of solutes in a bubble tube and how this affects their distribution in the surrounding sediment. Further, we investigate the influence of eddy diffusivity (i.e., bubble rise velocity), tube size, tube density in the sediment, and ebullition frequency on the mixing process, as well as its time dependence. Finally, methane gas fluxes are calculated based on the bubble-induced eddy diffusive mixing and the 3-D model parameters are translated into a 1-D representation of porewater irrigation.

2. METHODS

First, the geochemical analytical procedures are summarized in this section. Then, the 1-D transport-reaction model with its comprehensive reaction system, which is used to analyse the observed data, is described. Subsequently, the physically more realistic 3-D model for simulating the bubble-induced porewater mixing process is introduced, followed by linking the 3-D model parameters to the easy-to-use 1-D irrigation formula by Boudreau (1984). Finally, an expression is proposed to relate the mixing coefficient of the 3-D model to physically meaningful gas bubble characteristics, such as bubble radius, rise velocity, and methane fluxes.

2.1. Geochemical analytics

Surface sediment samples were retrieved using a gravity corer. The plastic liners were cut open and ~3 cm thick slices of sediment were taken in approximately 20–40 cm intervals. Subsequently, the porewater was extracted using a low-pressure squeezer (argon at 1–5 bar) at approximately in situ temperature of 4–8 °C in the ship's cold room. While squeezing the porewater was filtered through 0.2 μm cellulose acetate Nuclepore filters and collected in recipient vessels. Onboard, the collected porewater samples were analysed for their content of dissolved NH_4^+, H_2S, and total alkalinity (TA), whereas the analyses for SO_4^{2-} and Br^- were performed at the home laboratory. These porewater samples were stored refrigerated. In addition for home-based analyses, ~5 ml of wet sediment were collected for porosity and solid phase CNS (carbon, nitrogen, and sulphur) analyses, and an additional 5 ml of sediment was suspended in 20 ml of 1 N NaOH for methane headspace analyses. These samples were stored at room temperature.

Analyses of the dissolved porewater species NH_4^+ and H_2S followed standard chemical procedures (Grasshoff et al., 1999): Ammonium was measured as indophenol blue and sulphide as methylene blue, using a Hitachi UV/Vis spectrophotometer. Since high sulphide contents (>1 mM) interfere with the NH_4^+ analytics, these sub-samples were bubbled with argon for 1–3 h to strip any H_2S prior to the analysis. The total alkalinity of the porewater was determined by titration with 0.02 N HCl using the Tashiro indicator, a mixture of methyl red and methylene blue. The titration vessel was bubbled with nitrogen to strip any CO_2 and H_2S produced during the titration. The IAPSO (The International Association for the Physical Sciences of the Oceans) seawater standard was used for calibration of the method. The porewater sulphate and bromide content was determined by ion chromatography. Again, the IAPSO seawater standard was used for calibration. Porosity was determined by weight difference, before and after freeze drying the wet sediment sample and subsequently, transferred into a volume ratio (volume of porewater/volume of bulk sediment) assuming a dry sediment density of 2.5 g/cm^3 and a seawater density of 1.024 g/cm^3. Headspace methane was measured by gas chromatography (GC) using a flame-ionization detector (FID). Finally, the sedimentary organic carbon content was determined using a Carlo Erba element analyser.

2.2. Numerical 1-D model

The numerical 1-D transport-reaction model C.CANDI (Boudreau, 1996; Haeckel et al., 2001; Luff et al., 2001) was used to simulate the measured concentration-depth profiles of C_{org}, SO_4^{2-}, NH_4^+, H_2S, CH_4, total alkalinity (TA), and Br^- in order to analyse the geochemical situation in the sampled sediments. The general mathematical expressions

governing early diagenetic processes used in this numerical code were first advanced by Berner (1980):

$$\text{Solutes}: \frac{\partial \phi C}{\partial t} = \frac{\partial}{\partial x}\left(\phi D_S \frac{\partial C}{\partial x} - u\phi C\right) + \sum_j \phi R_j \quad (1a)$$

$$\text{Solids}: \frac{\partial (1-\phi) C}{\partial t} = \frac{\partial}{\partial x}(-w(1-\phi)C) + \sum_j (1-\phi) R_j \quad (1b)$$

where C is the concentration of a solute or solid, ϕ is the porosity, t is time, x is depth, D_S is the effective diffusion coefficient, u is the vertical advection velocity of the porewater, w is the sediment burial velocity, and ΣR_j represents the biogeochemical reactions the compound is involved. Since the sediments were anoxic, bioturbation was not an important transport process for solids and hence, it was not modelled.

The model then consists of a set of partial differential equations (PDEs), which are coupled by the reaction terms. In C.CANDI, the partial derivative with respect to depth, x, is approximated by block-centred finite differences, and the resulting set of ordinary differential equations (ODEs) is solved using the implicit ODE-solver VODE (Brown et al., 1989). Fast equilibrium reactions, such as protolytic reactions and dissolution–precipitation reactions, are expressed by non-linear algebraic equations and solved by the Newton–Raphson algorithm with a full Jacobian (Press et al., 1992). The concentrations in Eq. (1) are corrected for their thermodynamic equilibrium value at every time step (for details, see Luff et al., 2001).

Upper and lower boundary conditions were selected either as constant concentrations (Dirichlet condition) or constant gradients (Neumann or Robin condition) (for details, see Table 1). Model simulations were carried out in a time-dependent way until steady state (i.e., $\partial C/\partial t = 0$) was reached. Hence, the final model output should be independent of the initial conditions. Simulations of the background situation started with initial values based on the observed surface concentrations or linearly interpolated profiles between upper and lower boundary value. In contrast, the model simulations of the gas venting situation started from the steady state reference results.

An empirical relationship was least-squares fitted to the measured porosity data and imposed as a forcing function upon the model (Murray et al., 1978; Berner, 1980; Martin et al., 1991; Rabouille and Gaillard, 1991a,b):

$$\phi(x,t) = \phi_\infty + (\phi_0 - \phi_\infty)e^{-\beta x} \quad (2)$$

where ϕ_0 is the porosity at the sediment surface, ϕ_∞ is the porosity at infinite depth, and β is the porosity attenuation coefficient (see Table 2 for the fitted parameter values). Use of Eq. (2) assumes steady state compaction of the sediment.

The effective diffusion coefficients of solute compounds, D_S, were calculated from the molecular and ionic diffusion coefficients and corrected for salinity, pressure, and temperature according to Li and Gregory (1974) and using the Stokes–Einstein relation. Finally, the molecular diffusion coefficients were corrected for tortuosity using the expression $D_S = D_{mol}/(1-2\ln\phi)$ (Boudreau, 1997).

If we assume steady state compaction, then the sediment burial velocity, w, can be calculated as:

$$w(x) = \frac{1-\phi_\infty}{1-\phi} w_\infty \quad (3)$$

where w_∞ is the sediment burial velocity at infinite depth. Similarly, the porewater advection velocity at steady state compaction can be expressed as:

Table 1
Boundary conditions used in the 1-D and 3-D steady state modeling of the field data (background stations and vent sites)

Parameter [Unit]	3-D model	1-D model
Upper boundary conditions		
Labile C_{org} flux: F_{G_1} (x = 0, t) [μmol/(cm^2 a)]	—	15
Refractory C_{org} flux: F_{G_2} ($x = 0$, t) [μmol/(cm^2 a)]	—	25
$[SO_4^{2-}](x = 0, r, t)$[mM]	28	28
$[TNH_4](x = 0, r, t)$ [mM]	0	0
$[TH_2S](x = 0, r, t)$ [mM]	0	0
$[TCO_2](x = 0, r, t)$ [mM]	2.2	2.2
$[TA](x = 0, r, t)$ [meq/l]	2.4	2.4
$[CH_4](x = 0, r, t)$ [mM]	0	0
$[Br^-](x = 0, r, t)$ [mM]	0.84	0.84
Lower boundary conditions		
$dC/dx\|_{x=L,r,t}$ [mM/cm]	0	0
$[TNH_4]$ (x=L,r,t) [mM][a]	4.9	—
$[CH_4](x = L, r, t)$ [mM][b]	15	100
Left boundary conditions		
$dC/dr\|_{x,r=0,t}$ [mM/cm]	0	—
Right boundary condition		
$dC/dr\|_{x,r=r_2,t}$ [mM/cm]	0	—

C = respective concentration of solute or solid compound.

[a] A Dirichlet boundary condition was only used for TNH_4 in the 3-D bubble mixing realizations. For the reference model simulation, a Neumann boundary condition was used.

[b] A Dirichlet boundary condition was only used for CH_4 in the 3-D reference simulation and the 1-D bubble irrigation simulations. In all other model runs Neumann boundary conditions were used.

Table 2
Parameter values used in the 1-D and 3-D model simulations

Parameter [Unit]	3-D model	1-D model
Maximum depth of calculation: L [cm]	600	1000
Number of vertical layers	150	1000
Number of horizontal layers	51	—
Length of bubble tube: x_T [cm]	300[a]	—
Irrigation depth: x_{irr} [cm]	—	300[a]
Irrigation coefficient: α [a^{-1}]	—	0.1[a]
Porosity at $x = 0$: ϕ_0	0.82(3)[b]	0.82(3)[b]
Porosity at $x = \infty$: ϕ_∞	0.781(4)[b]	0.781(4)[b]
Porosity attenuation coefficient: β [cm^{-1}]	0.04(4)[b]	0.04(4)[b]
Sediment burial velocity at $x = \infty$: w_∞ [cm/a]	0.05[c]	0.05[c]
C_{org} concentration at $x = 0$: G_0 [wt%]	1.65(5)[d]	—
C_{org} concentration at $x = 600$: G_L [wt%]	1.26(14)[d]	—
Attenuation of C_{org} degradation rate: γ [cm^{-1}]	0.004(3)[d]	—
Rate constant for labile C_{org} degradation: k_{G_1} [a^{-1}]	2×10^{-5}	1×10^{-4}
Rate constant for refractory C_{org} degradation: k_{G_2} [a^{-1}]	—	1×10^{-5}
Organic matter composition (C:N:Br)	106:16:0.4	106:16:0.4
Monod and inhibition constant for SO_4^{2-}: K_{SO_4} [mM]	1[e]	1[e]
Rate constant for AMO: k_{AMO} [$mM^{-1}\,a^{-1}$]	1×10^6	1×10^4

[a] Parameters are only used in the respective 1-D or 3-D simulations of bubble-induced irrigation.
[b] Results of least-squares fit to all porosity data ($\chi^2 = 0.18$) with 2σ standard deviation given in brackets (last digit).
[c] Approximated mean of values found in the literature (Nürnberg and Tiedemann, 2004; Wallmann et al., 2006a).
[d] Results of least-squares fit to all background C_{org} data ($\chi^2 = 0.33$) with 2σ standard deviation given in brackets (last digit).
[e] For example, Van Cappellen et al. (1993) and Boudreau (1996).

$$u(x) = \frac{\phi_\infty}{\phi} w_\infty \tag{4}$$

This representation assumes that no external forces exist, which induce additional fluid advection. Our field data do not indicate upward fluid flow at the vent sites (see Section 4.1.2 for the discussion) and hence, our simplification is warranted.

Organic matter (C_{org}) was modelled as two fractions (2-G model), a labile (G_1) and a refractory (G_2) component. Degradation of the organic material followed first-order kinetics with respect to C_{org} concentrations (G_1 and G_2) and the microbial mediation was described by Monod-type functions and inhibition terms. Since the reference stations are dominated by anoxic conditions, only sulphate reduction (SR) and methanogenesis (M) were considered as degradation pathways:

$$\begin{aligned}(CH_2O)_a(NH_3)_b(H_3PO_4)_c(Br^-)_d + \frac{a}{2}SO_4^{2-} \\ \rightarrow \frac{a}{2}HCO_3^- + \frac{a}{2}CO_2 + \frac{a}{2}HS^- + bNH_3 + cH_3PO_4 \\ + dBr^- + \frac{a}{2}H_2O\end{aligned} \tag{5}$$

$$\begin{aligned}(CH_2O)_a(NH_3)_b(H_3PO_4)_c(Br^-)_d \\ \rightarrow \frac{a}{2}CH_4 + \frac{a}{2}CO_2 + bNH_3 + cH_3PO_4 + dBr^-\end{aligned} \tag{6}$$

where a, b, c, and d represent the stoichiometry of the organic matter composition with respect to carbon, nitrogen, phosphorus, and bromine.

The respective rate laws for sulphate reduction (Eq. (5)) and methanogenesis (Eq. (6)), R_{SR} and R_M, are:

$$R_{SR} = \sum_i k_{G_i} G_i \frac{[SO_4^{2-}]}{K_{SO_4} + [SO_4^{2-}]} \tag{7}$$

and

$$R_M = \sum_i k_{G_i} G_i \frac{K_{SO_4}}{K_{SO_4} + [SO_4^{2-}]} \tag{8}$$

where k_{G_i} is the rate constant for organic matter degradation with respect to each fraction, i, of the organic matter (i.e., G_1 and G_2) and K_{SO_4} is the Monod constant for sulphate reduction of C_{org}. In Eq. (8), we assume that the value of the inhibition constant for methanogenesis due to sulphate reduction equals the value of the Monod constant K_{SO_4}.

As the only additional reaction affecting dissolved compounds reported in this study, anaerobic methane oxidation (AMO) was included:

$$CH_4 + SO_4^{2-} \rightarrow HCO_3^- + HS^- + H_2O \tag{9}$$

Mathematically, a second-order rate law describes this redox reaction (Van Cappellen and Gaillard, 1996; Van Cappellen and Wang, 1996):

$$R_{AMO} = k_{AMO}[CH_4][SO_4^{2-}] \tag{10}$$

where k_{AMO} is the rate constant for AMO.

The resulting reaction terms, ΣR_j, of Eq. (1) for each transported compound displayed in Figs. 4 and 5 are given in Table 3. Most model parameters were adjusted to reproduce the observed field data and some are literature-based (see Table 2 for details).

The kinetically controlled reactions above (Eqs. (5), (6), and (9)) release or consume protolytic compounds, such as bicarbonate and hydrogen sulphide, that undergo fast dissociation reactions, which are thermodynamically controlled. In the 1-D model simulations with C.CANDI the 'alkalinity conservation approach' (Boudreau, 1987; Boudreau and Canfield, 1988; Luff et al., 2001) was used

Table 3
Reaction rate terms, ΣR_j, for each compound considered in the numerical 1-D and 3-D models

Compound	$\Sigma R_j =$
C_{org}	$-R_{SR}-R_M$
SO_4^{2-}	$-1/2\ R_{SR}-R_{AMO}$
CH_4	$1/2\ R_M-R_{AMO}$
TNH_4	$b/a\ (R_{SR}+R_M)$
Br^-	$d/a\ (R_{SR}+R_M)$
$TH_2S/\ HS^-/\ HCO_3^-$	$1/2\ R_{SR}+R_{AMO}$
TCO_2	$R_{SR}+1/2\ R_M+R_{AMO}$
TA	$R_{SR}+2\ R_{AMO}$

Note: The concentrations of C_{org} (G) were converted from wt% into mM prior to the calculations. Thus, the factor, $\rho_S/M_W\times(1-\phi)/\phi\times10^4$, was applied, where ρ_S is the dry density of the sediment (i.e., 2.5 g/cm^3) and M_W is the molar weight of carbon (i.e., 12 g/mol).

to correct for the disequilibrium arising from the formulation of the kinetic reactions. Thus, the sum parameters TCO_2, TH_2S, and TA,

$$\begin{aligned} TCO_2 &= [HCO_3^-] + [CO_3^{2-}] + [CO_2] \\ TH_2S &= [HS^-] + [H_2S] \\ TA &= [HS^-] + [HCO_3^-] + 2[CO_3^{2-}] \end{aligned} \tag{11}$$

were transported and reacted in the numerical model. The respective diffusion coefficients and concentration gradients were calculated from values for the individual species. The equilibrium constants of the acid–base reactions were calculated using empirical functions that account for their dependence on pressure, temperature, and salinity (Millero, 1983; Clegg and Whitfield, 1995; Millero, 1995). For a detailed description on the alkalinity and pH treatment in C.CANDI, please refer to Luff et al. (2001).

2.3. Numerical 3-D model

A transient 3-D finite-difference transport-reaction model was developed to simulate the mixing of porewater caused by gas bubbles rising through the sediment. In the model realizations the influence of various parameters (Table 4) characteristic for the gas bubble transport process, such as bubble radius, spacing between bubble tubes, mixing coefficients, and time of mixing, on the distribution of dissolved porewater constituents were tested. Ammonium was chosen as representative dissolved species to investigate the bubble mixing process. The numerical grid is continuous, but consists of two domains (Fig. 1a): (a) an inner domain representing the bubble tube with radius r_1 and (b) an outer domain representing the sediment surrounding the tube. Hence, neighbouring tubes have a distance between their outer walls of $2(r_2-r_1)$. As a first approximation and due to computational costs, a cylindrical bubble tube geometry was chosen, though it is known that bubbles grow in oblate spheroidal shapes (Johnson et al., 2002; Gardiner et al., 2003). It is further assumed that radial symmetry exists which simplifies the mathematical problem to solving a set of two-dimensional non-linear partial differential equations (PDE). Thus, the respective equations solved simultaneously for both domains are:

(a) sediment domain:

$$\frac{\partial\phi C}{\partial t} = \frac{\partial}{\partial x}\left(\phi D_S\frac{\partial C}{\partial x} - u\phi C\right) + \frac{1}{r}\frac{\partial}{\partial r}\left(\phi D_S r\frac{\partial C}{\partial r}\right) + \sum_j \phi R_j \tag{12a}$$

(b) tube domain:

$$\frac{\partial\phi C}{\partial t} = \frac{\partial}{\partial x}\left(\phi(D_S+K_{eddy})\frac{\partial C}{\partial x} - u\phi C\right) + \frac{1}{r} \times \frac{\partial}{\partial r}\left(\phi(D_S+K_{eddy})r\frac{\partial C}{\partial r}\right) + \sum_j \phi R_j \tag{12b}$$

where C is the concentration of the dissolved constituent, D_S is the effective diffusion coefficient (radial and vertical components are assumed identical), K_{eddy} is the bubble-related eddy diffusion coefficient, u is the vertical porewater advection velocity, ΣR_j are the diagenetic reactions rates of the porewater constituent, ϕ is the porosity, t is the time, x is the depth, and r is the radial distance from the tube centre.

The publicly available algorithm PDETWO (Melgaard and Sincovec, 1981a,b) was chosen to solve this time-dependent problem. The solver approximates the PDE system spatially with a five-point differencing scheme and solves it in conjunction with the ODE integrator GEARB. Neumann boundary conditions were chosen for the left and right boundary, while a combination of Dirichlet and Neumann conditions was applied to the upper and lower boundary of the model grid (see Table 1). The initial condition for the model realizations simulating bubble mixing was provided by the steady state simulation of the reference situation. In this model simulation without gas venting the same porewater constituents as in the 1-D model were included. The radial resolution was chosen such that the tube always consisted of a minimum of 5 grid points. The total number of grid points in the radial direction was always 51. Hence, the lateral resolution of the sediment domain was dependent on the total size of the domain. Vertically,

Table 4
Parameter variations in the 3-D model realizations of continuous bubble streams

Parameter [unit]	Range of values
Radius of bubble tube, r_1 [cm]	0.05; 0.1; 0.5; 1; 5; 10
Radius of total model domain, r_2 [cm]	0.5; 1; 5; 10; 20; 50; 100; 200
Time, t [a]	0.0001; 0.001; 0.01; 0.1; 0.5; 1; 5; 10; 20; 50
Eddy diffusivity, K_{eddy} [cm^2/a]	1×10^4; 5×10^4; 1×10^5; 5×10^5; 1×10^6; 5×10^6; 1×10^7; 5×10^7; 1×10^8; 5×10^8; 1×10^9

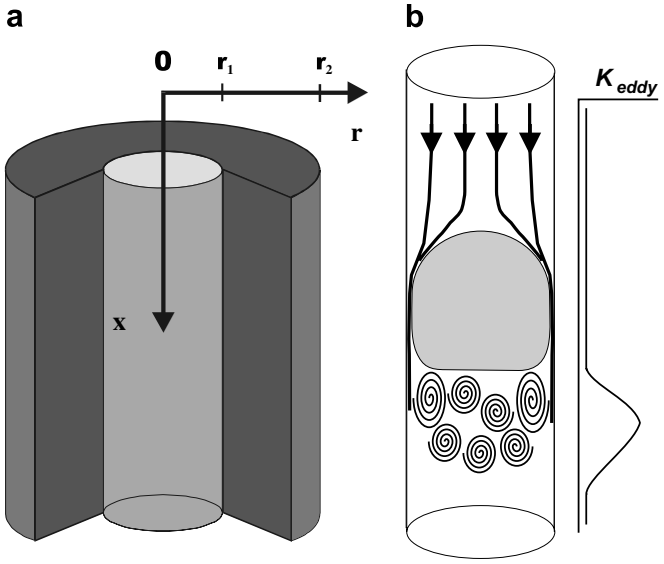

Fig. 1. (a) 3-D cylindrical geometry of the numerical model. The model grid consists of 2 domains, representing the gas bubble tube (light grey) of radius r_1 and the surrounding sediment (dark grey). The spacing between adjacent tubes is $2(r_2 - r_1)$. (b) Schematic sketch of a single bubble rising in a tube. Streamlines indicate flow of water relative to bubble; vortices indicate turbulence in the wake of the bubble. The attached graph sketches the depth distribution of the corresponding eddy diffusion coefficient according to Eq. (18).

151 grid points were always used, and thus, the resolution was 4 cm as 600 cm were modelled in total.

The vertical porosity distribution was prescribed in the model using Eq. (2) and the parameter values of the least-squares fit to the data (Table 2). The porosity was assumed to be laterally homogeneous in the sediment domain. In the tube domain, porosity was set to 1, because the bubble tube is filled with water.

Radial advection was neglected in the model, as was the vertical porewater velocity, u, arising from sediment burial, w_∞ (Eq. (4)). Since sediment burial velocities in the Sea of Okhotsk are generally below 100 cm/ka (Nürnberg and Tiedemann, 2004; Wallmann et al., 2006a), porewater advection rates are about 2 orders of magnitude smaller than the other rate terms in Eq. (12). Also, any diagenetic reaction in the bubble tube was disregarded (i.e., $\Sigma R_j = 0$). In the tube domain, the apparent diffusion coefficient represented a combination of eddy diffusion and molecular diffusion ($K_{\mathrm{eddy}} + D_{\mathrm{mol}}$), while molecular diffusion prevailed in the sediment domain. The molecular diffusion coefficient was corrected for salinity, temperature, and pressure according to Li and Gregory (1974) and the Stokes–Einstein relation. Finally, the molecular diffusion coefficient was also corrected for tortuosity using the expression $D_{\mathrm{S}} = D_{\mathrm{mol}}/(1-2\ln\phi)$ (Boudreau, 1997).

In the sediments, organic matter is degraded according to a first-order rate law with respect to the concentration of C_{org}. Since solid compounds were not explicitly modelled in the 3-D calculations of this study, the measured organic matter concentration profile, $G(x)$, was prescribed using a depth-dependent function:

$$G(x) = G_L + (G_0 - G_L)\mathrm{e}^{-\gamma x} \tag{13}$$

where G_0 is the organic matter concentration at the sediment surface, G_L is the organic matter concentration at a sediment depth of $L = 600$ cm, and γ determines the exponential decrease of C_{org} with depth (see Table 2 for the resulting parameter values of the least-squares fit).

To keep computational costs to a minimum no thermodynamic equilibrium calculations were performed in the 3-D model. Thus, bicarbonate represents TCO_2 and hydrogen sulphide represents TH_2S. Total alkalinity was simply calculated from the concentrations of bicarbonate and hydrogen sulphide (i.e., $TA = [HCO_3^-] + [HS^-]$). However, the two ions were transported and reacted separately in the model and not as a summed variable.

Other parameter and variable choices are based on field data from the north-eastern shelf of Sakhalin Island, Sea of Okhotsk (see Table 2 and Section 4.1).

2.4. 1-D approximation of porewater irrigation

In order to provide an easy-to-use expression for simulating the porewater irrigation due to gas bubble rise in soft sediments, Aller's bioirrigation model (Aller, 1980) has been adopted. In one dimension, the radial component of Eq. (12) can be reduced, under appropriate conditions, to a simple source–sink term (Boudreau, 1984):

$$\frac{\partial \phi \overline{C}}{\partial t} = \frac{\partial}{\partial x}\left(\phi D_{\mathrm{S}} \frac{\partial \overline{C}}{\partial x} - u\phi\overline{C}\right) + \phi\alpha(\overline{C} - C_r) + \sum_j \phi \overline{R}_j \tag{14}$$

where $\overline{C}$ is the radially averaged concentration, C_r the concentration at the tube wall, and α is the irrigation coefficient (i.e., the fraction of solute exchanged per unit time) (Boudreau, 1984):

$$\alpha(x,t) = \frac{2r_1\phi D_{\mathrm{S}}}{(r_2^2 - r_1^2)(\bar{r} - r_1)} \quad (r_1 < \bar{r} < r_2) \tag{15}$$

where r_1 and r_2 are the same radii as defined in our cylindrical model geometry (Fig. 1a).

Eq. (14) assumes that the gas bubbles are mixing on a much faster time scale than solutes are transported by molecular diffusion and advection, and thereby 'instantaneously' mix the tubewater to keep it at bottom-water concentrations (i.e., $C_r = C_0$). The irrigation coefficient, α, provides some information on the spatial distribution (r_2) and size of the bubble tubes (r_1), while the eddy diffusivity assigned to the 3-D bubble mixing process also provides information about the gas flux (as outlined in Section 2.5). Thus, a K_{eddy} can be translated into an α-value using the definition in Eq. (15). The other way around, the above assumption of instantaneous flushing of the tube (Eq. (14)) requires a certain K_{eddy} value (as demonstrated in Section 4.3). An estimate of the minimum gas flux necessary to keep the tube well-flushed at bottom-water concentrations, C_0, based on an α-value is thus possible. However, α is generally a fitting parameter and the associated geometry is unknown.

Recently, Grigg et al. (2005) and Meile et al. (2005) reviewed the equivalence of the above non-local 1-D representation with 3-D cylinder models and discussed the limits. Grigg et al. (2005) stated that Eq. (14) is ideally suited for simple reaction kinetics (e.g., non-linear reaction terms can be radially averaged, no radial dependence of the reaction term). These authors also advanced other expressions for α that could be related to parameters of our 3-D model under certain assumptions. In addition, Meile et al. (2005) report that not only the irrigation coefficients are highly solute-specific because of the variable reactivities of the porewater constituents, but also the 1-D representation is affected by the three-dimensional chemical dynamics created by flushing of the burrows and tubes.

2.5. Gas bubble rise and eddy diffusion

In our 3-D model, we assume that initial gas bubbles have already formed the tubes in which the subsequent bubbles rise. It is beyond the scope of this study to derive a formula for the speed of the initial crack formation and propagation in soft sediments. Instead, we assume that a sequence of bubbles has already created an enlarged bubble tube in sediments, which is greater than a bubble diameter and acts like a pipe (Fig. 1). Davies and Taylor (1950) have shown that gas bubbles, which ascend through a pipe filled with water, reach a terminal rise velocity, u_{rise}, proportional to the bubble radius, r_{bubble}. They derived a theoretical relationship that closely matched the experimental results:

$$u_{rise} = 0.464\sqrt{g \cdot r_{bubble}} \quad (16)$$

where g is the acceleration due to gravity ($g = 9.81$ m/s^2).

Furthermore, Prandtl and Tietjens (1957) state that an eddy diffusion coefficient (K_{eddy}) for turbulent mixing is proportional to the velocity of the wave (v) times its mixing length (d): $K_{eddy} \propto vd$. A gas bubble rising in a tube completely mixes a volume of water equivalent to its own volume at any time (Fig. 1b). Hence, the mixing length is equivalent to the diameter of the bubble, d_{bubble}. Thus, applying Prandtl's mixing length theory to Taylor's equation (Eq. (16)) and assuming a proportionality of 1 provides a first-order estimate of the maximum eddy diffusivity caused by a bubble rising in a tube (see also Fig. 2a):

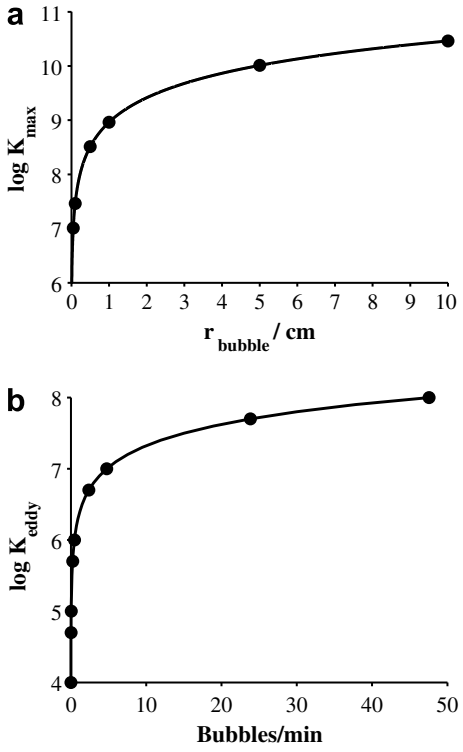

Fig. 2. Eddy diffusion coefficient as a function of (a) bubble radius (Eq. (17)) and (b) bubble frequency (Eq. (20) and a bubble radius of 1 cm). The theoretical relationships are based on the definition of the terminal rise velocity of bubbles in pipes (Eq. (16)) after Davies and Taylor (1950) and Prandtl's turbulent mixing length theory (Prandtl and Tietjens, 1957). Dots represent parameter values used in the 3-D model realizations.

$$K_{eddy} \approx u_{rise} \cdot d_{bubble} = 0.928\sqrt{g \cdot r_{bubble}^3} \quad (17)$$

Hence, we also imply that the diameter of the rising gas bubbles is equivalent to the size of the initial tube. Davies and Taylor (1950) used a straight glass pipe to develop Eq. (16), but bubbles can follow a curved path when rising in sediments (Boudreau et al., 2005). Eq. (17) will give a theoretical maximum for the eddy diffusion coefficient. Thus, Eqs. (16) and (17) provide us with the means to relate the eddy diffusion coefficient used in the model realizations to bubble rise velocities and tube geometry.

Generally, surface porewaters are undersaturated with respect to methane and methane bubbles will shrink and dissolve. We show that high eddy diffusivities, i.e. high rise velocities, are necessary in order to observe a mixing effect. Hence, the interaction time between gas bubble and porewater is short and thus, the shrinking of gas bubbles was neglected in this study.

While Eq. (17) represents a continuous stream of bubbles, in natural settings gas ebullition is generally observed in discrete pulses of gas bubbles with intermediate intervals of quiescence (Martens et al., 1980; Martens and Klump, 1980; Leifer et al., 2004). In our model we approximated these bubble pulses by assigning a Gaussian distribution to the eddy diffusivity as a function of depth and time:

$$K_{\text{eddy}} = K_0 e^{-\left(\frac{x-u_{\text{rise}}t}{\sigma}\right)^2} \quad (18)$$

where K_0 is the eddy diffusion constant in the centre of the pulse, σ is a measure of the width of the bubble pulse, and u_{rise} is the bubble rise velocity. Hence, $u_{\text{rise}}t$ gives the sediment depth of the bubble pulse as a function of time. This smooth function was preferred over a rectangular function in order to facilitate the numerical integration of the problem of pulsed bubble ebullition. Thus, a period of bubble ebullition, where eddy diffusivities prevail in the tube, is followed by a period of quiescence, where mixing is reduced to molecular diffusion only (Fig. 1b). The average value of K_{eddy} over the tube length and simulation time can be calculated using the mean value theorem for integrals:

$$\langle K_{\text{eddy}} \rangle = \frac{\iint K_{\text{eddy}}\,dx\,dt}{\iint dx\,dt} = K_0 \frac{\iint \exp\left(-\left(\frac{x-u_{\text{rise}}t}{\sigma}\right)^2\right) dx\,dt}{\iint dx\,dt} \quad (19)$$

Finally, the previous discussions allow us to translate the $\langle K_{\text{eddy}} \rangle$ value into a bubble frequency (i.e., the number of gas bubbles leaving the sediment per time interval) and thus, into a gas flux. Since the rise velocity, u_{rise}, provides us with the total time of rise, t_{rise}, for a given tube length, x_T, and continuous bubble streams require a certain amount of bubbles, n_{bubble}, with diameter, d_{bubble}, in the tube, Eq. (17) can be written as:

$$\langle K_{\text{eddy}} \rangle \approx u_{\text{rise}} \cdot d_{\text{bubble}} = d_{\text{bubble}}^2 \frac{n_{\text{bubble}}}{t_{\text{rise}}} \quad (20)$$

Fig. 2b displays a semi-logarithmic plot of Eq. (20) as a function of the bubble frequency, i.e., $f_{\text{bubble}} = n_{\text{bubble}}/t_{\text{rise}}$, for a bubble radius of $r_1 = 1$ cm. The dots represent the eddy diffusivities of continuous bubble streams that were used in our model. The bubble frequency can easily be translated into a methane flow by multiplying with the average volume of a gas bubble, V_{bubble}:

$$F_{CH_4} = f_{\text{bubble}} \cdot V_{\text{bubble}} = \frac{\langle K_{\text{eddy}} \rangle}{4r_{\text{bubble}}^2} V_{\text{bubble}} \left[\frac{\text{volume}}{\text{time}}\right] \quad (21)$$

3. SITE DESCRIPTION

The joint German–Russian project KOMEX (Kurile-Okhotsk Sea Marine Experiment) (Biebow and Hütten, 1999; Biebow et al., 2000) discovered several vent sites on the north-eastern slope and shelf of Sakhalin Island, Sea of Okhotsk (Fig. 3). Numerous hydro-acoustic anomalies (commonly called 'gas flares') caused by gas bubbles in the water column, as well as elevated methane concentrations in bottom-waters, indicate active gas venting (Obzhirov et al., 2004). These flares have been observed during the last 20 years, and methane emissions are reported to have increased during this time, due to periods of seismo-tectonic activity (Obzhirov et al., 2004). Water column methane concentrations reach 400–800 nM of methane (i.e., 10,000–20,000 nl/l at a pressure of 1 atm) in the flares compared to background concentrations of less than 5 nM of methane (i.e., <100 nl/l at a pressure of 1 atm), and flares rise as high as 300–400 m above the seafloor (Obzhirov et al., 2004).

Gas emissions from vent sites, as well as mud volcanoes at the Sakhalin slope, are likely activated by tectonic movements along the transform plate boundary which separates the Okhotsk Sea plate from the Eurasian and Amur plates (Shakirov et al., 2004). The tectonic activity provides a

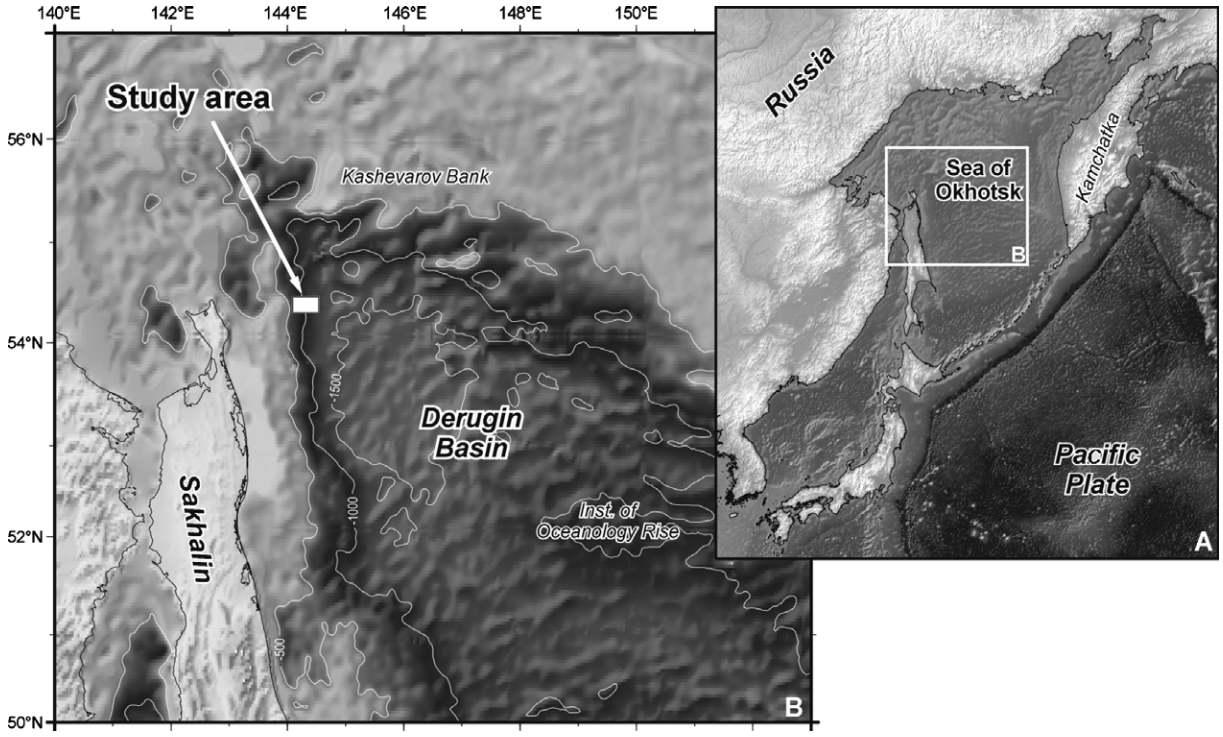

Fig. 3. Map of the Sea of Okhotsk showing the study area, Obzhirov Flare, northeast off Sakhalin.

Table 5
Sampling locations on the northeastern Sakhalin shelf, Sea of Okhotsk

Core	Latitude (N)	Longitude (E)	Water depth/m	Remarks
LV 28 20-2	54°26.519′	144°04.093′	685	Background
GE 99 26-2	54°31.176′	144°05.276′	700	Background
GE 99 24-2	54°26.662′	144°04.517′	700	Seep
GE 99 27-2	54°26.663′	144°04.812′	690	Seep
GE 99 29-3	54°26.784′	144°04.765′	700	Seep

complicated setting of folded and disrupted strata. In addition, the northern slope and shelf of Sakhalin Island are strongly influenced by sediment input from the Amur River. Primary production is high, reaching values of 250 g/(m^2 a) of carbon (Antoine et al., 1996), and Holocene sediment burial velocities can be as high as 0.1 cm/a (Wong et al., 2003).

This combination of tectonic activity, opening up deep faults, and high organic carbon content leads to methane accumulation in the sediments and allows for the formation of methane hydrates in surface sediments as well as a pronounced bottom-simulating reflector (BSR) throughout the northern slope area off Sakhalin Island (Lüdmann and Wong, 2003). A BSR marks the lower boundary of the gas hydrate stability zone. Methane hydrates sampled in surface sediments of active vent sites in this area are predominately of biogenic origin (Ginsburg et al., 1993; Matveeva et al., 2003).

4. RESULTS AND DISCUSSION

First, we will present a geochemical analysis of the observed data using the 1-D model, before the 3-D analysis of the bubble-induced mixing process is discussed. This is followed by a sensitivity analysis of the 3-D model parameters and a discussion of pulsed bubble ebullition versus continuous streams of bubbles. Finally, methane gas fluxes are calculated from the model parameters and the 3-D parameters are related to a 1-D representation of porewater irrigation.

4.1. Steady state modelling of the geochemical data

During two sampling campaigns with the RV Akademik M. A. Lavrentyev (cruise LV-28 in 1998) and the MV Marshal Gelovany (cruise GE-99, in 1999) several gravity cores were taken in an area called 'Obzhirov Flare' (Table 5) at a water depth of ~700 m, where emissions of free methane gas had been observed in the water column (Obzhirov et al., 2004). As a result of the methane flux, the vent sites are characterized by extremely high enrichments of sulphide and methane in the porewater, carbonate precipitation, near-surface gas hydrate formation, and a chemoautotrophic fauna typical of vent sites where reduced geochemical substances escape.

The gravity cores exhibit two different types of porewater profiles. Type I reflects the background situation of anoxic degradation of organic material (Fig. 4), whereas type II indicates intense irrigation of bottom-water concentrations into depth (Fig. 5). Steady state simulations were performed with the comprehensive numerical 1-D transport-reaction model C.CANDI (dashed lines in Figs. 4 and 5). In addition, the model output of 3-D simulations, which are discussed later in the text, is also shown (solid lines in Figs. 4 and 5).

4.1.1. Background situation

Early diagenesis in sediments of two background gravity cores, LV28 20-2 and GE99 26-2, is controlled by anaerobic degradation of particulate organic carbon (POC) (Fig. 4). Due to high productivity and sediment input from the Amur river, sediment burial velocities are generally high (10–100 cm/ka) (Nürnberg and Tiedemann, 2004; Wallmann et al., 2006a), and thus POC contents are about 1.65 wt% close to the sediment surface and decrease to ~1.26 wt% within the upper 600 cm of the sediment (Fig. 4 and Table 2). The results of the 1-D model (dashed lines) suggest a total flux of 40 μmol/(cm^2 a) of carbon into the anoxic sediments (Table 1). Organic matter degradation in the reference sediments is well reproduced by considering 2 fractions (2-G model) of relatively low reactivity. Rate constants of $k_{G_1} = 1 \times 10^{-4}\,a^{-1}$ and $k_{G_2} = 2 \times 10^{-5}\,a^{-1}$ reproduce the measured concentrations best.

During the mainly anoxic degradation of organic matter considerable amounts of NH_4^+ as well as Br^- are released. The concentrations of these compounds steadily increase with depth and do not reach an asymptotic concentration at 600 cmbsf (centimeter below seafloor). The respective concentration increases amount to: $\Delta[NH_4^+] = 5$–6 mM and $\Delta[Br^-] = 100$–150 μM. Applying a Redfield ratio of 106:16 (C:N) and a Neumann condition for NH_4^+ at the bottom boundary reproduces the C_{org} and NH_4^+ data quite well (dashed line in Fig. 4). Sulphate becomes completely depleted at a sediment depth of 200–300 cm and, as a consequence, methanogenesis begins at this depth. Therefore, only sulphate reduction and methanogenesis are considered as pathways for POC degradation in the numerical model, and microbial methane production is simulated down to a sediment depth of 1000 cm. At that depth, a Neumann bottom boundary condition is imposed on the 1-D model (see Table 1). A 1-D simulation (not shown) also predicts the depth of methane saturation with gas hydrates (~59 mM according to Tishchenko et al. (2005)) to be at least 60 m below the seafloor.

The linearity of the sulphate profile indicates a hot spot of methane oxidation by sulphate (AMO). The depth profiles also indicate a steady state situation for the compounds involved in this reaction. This gives a total flux of sulphate from above of ~15 μmol/(cm^2 a). The numerical model runs revealed that ~90% of the sulphate flux is balanced by the CH_4 flux from below and only ~10% is related to POC degradation. Consequently, sulphide and alkalinity values also

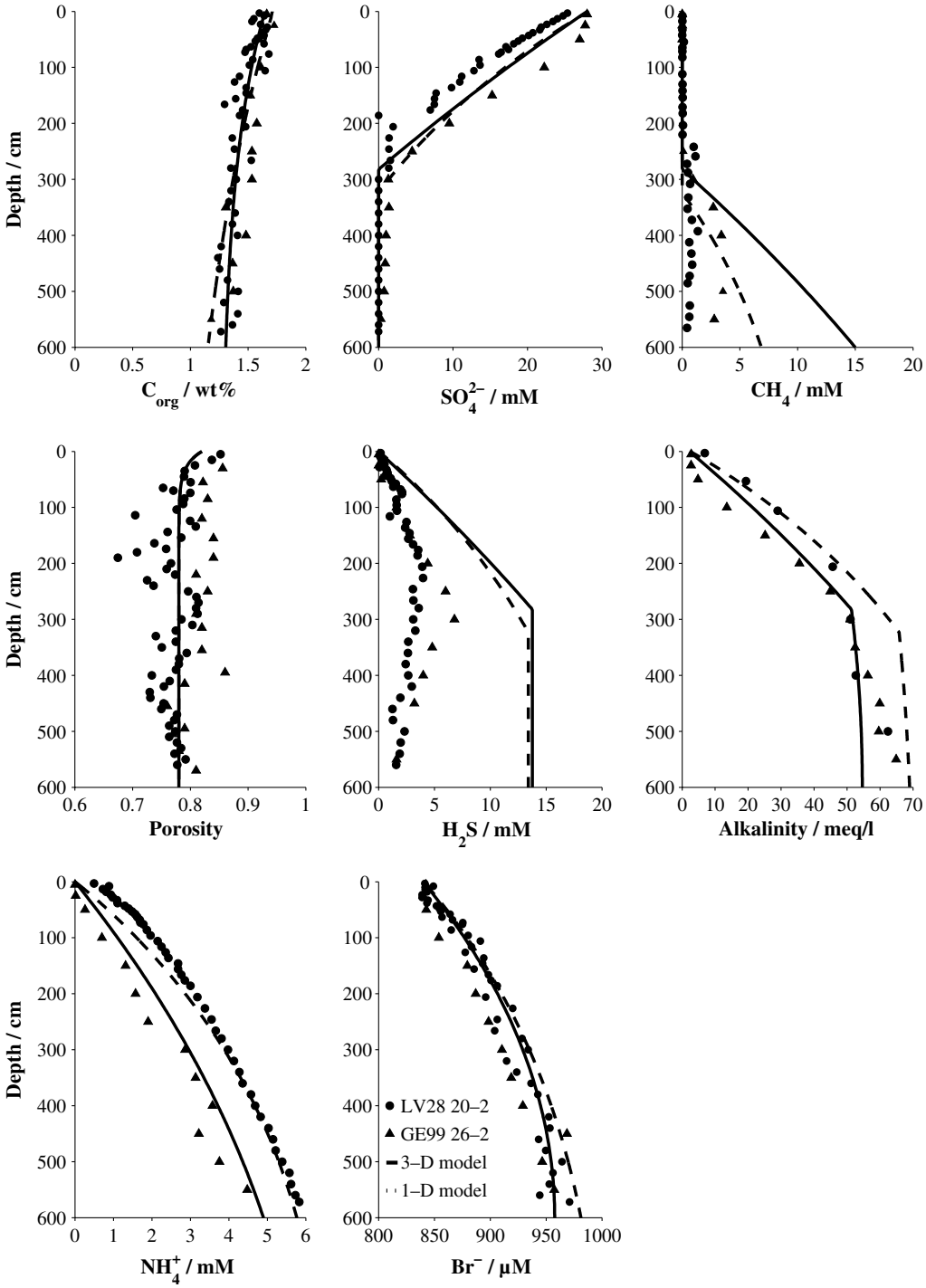

Fig. 4. Biogeochemical background situation ('no venting') in the sediments of the Obzhirov Flare area. Solid symbols represent the observed field data of C_{org}, SO_4^{2-}, CH_4, porosity, H_2S, TA, NH_4^+, and Br^-. The steady state results of the numerical analyses are given by the lines: (a) solid—radially averaged 3-D profiles and (b) dashed—1-D model. Note, that the observed methane concentrations are largely altered during core recovery and sampling, and they do not reflect in situ concentrations.

increase linearly within the upper 300 cm of the sediment, because they are primarily produced by AMO in this interval. Below the AMO reaction front at ~300 cmbsf, the gradient of both variables changes drastically, because methanogenesis produces very little to no alkalinity and no sulphide. The discrepancy between the observed sulphide concentrations and the modelled profiles (1-D and also 3-D) is most likely the result of the formation of iron sulphides, which remove dissolved sulphide from the porewater. This process was not included in the model simulations.

In general, the importance of AMO and POC degradation on sulphate reduction seems to be highly variable in

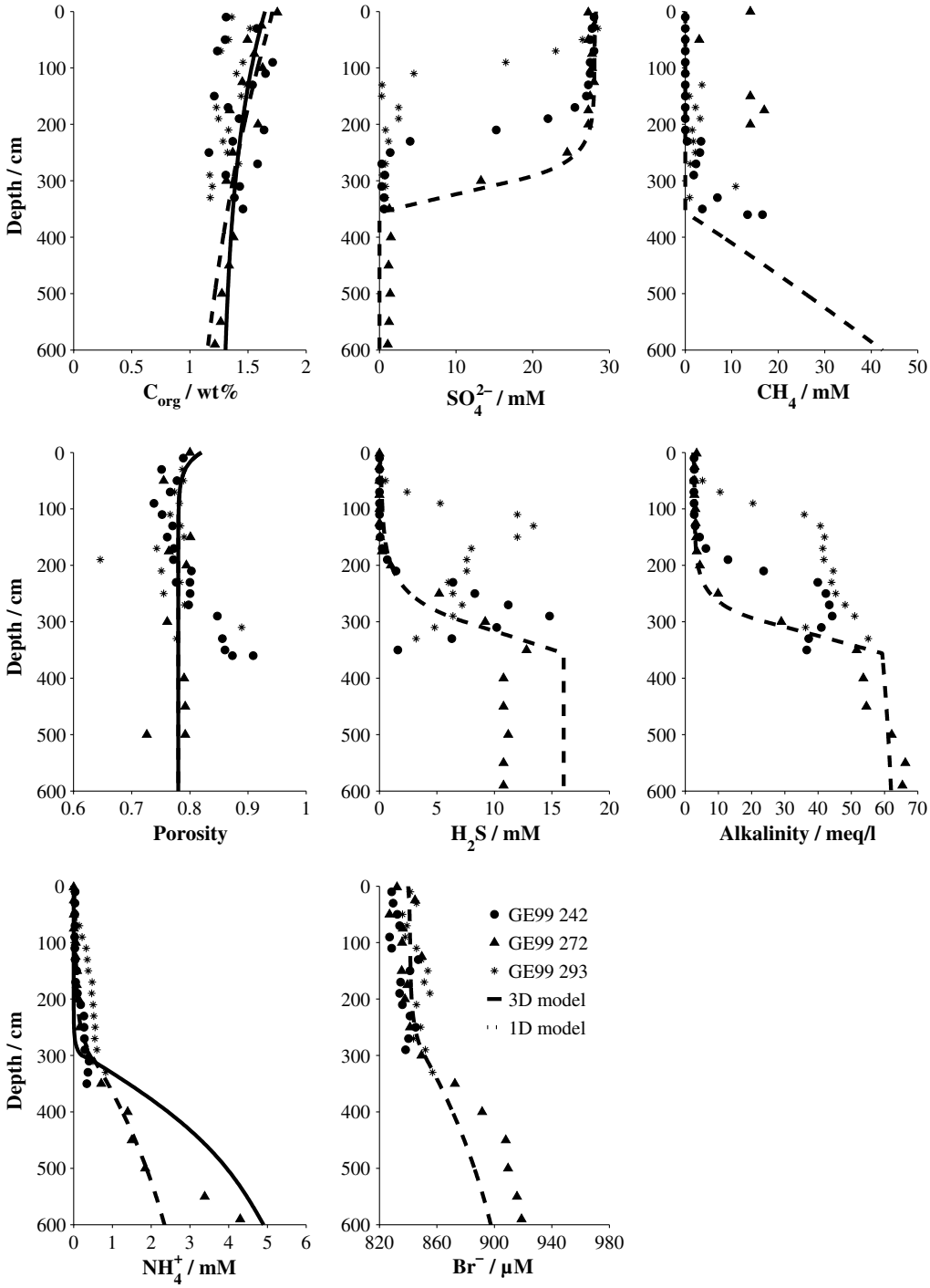

Fig. 5. Biogeochemical situation at the vent sites with active methane gas ebullition in the Obzhirov Flare area. Solid symbols represent the observed field data of C_{org}, SO_4^{2-}, CH_4, porosity, H_2S, TA, NH_4^+, and Br^-. The lines depict the results of the numerical analyses: (a) solid – example result of the 3-D bubble mixing model (only NH_4^+; see Table 2 and Fig. 6 for tube geometry) and (b) dashed – steady state result of the 1-D irrigation model. Note, that the observed methane concentrations are largely altered during core recovery and sampling, and they do not reflect in situ concentrations. Cores 24-2 and 29-3 recovered the top of a gas hydrate layer in a sediment depth of ~300 cm.

sediments at continental margins. While Fossing et al. (2000) and Jørgensen et al. (2001) found that the major fraction of sulphate in sediments off Namibia and in the Black Sea, respectively, was consumed by POC degradation, Niewöhner et al. (1998) report that almost 100% of the sulphate is consumed by AMO in slope sediments off Namibia. A similar range has been reported for Sakhalin slope sediments (Wallmann et al., 2006a) with an average of 40% consumed by AMO. Our model determines a maximum AMO rate of ~300 mM/a that is comparable to the maximum rates measured in experiments by Fossing et al. (2000).

4.1.2. Gas flare situation

The second type of porewater profiles shows bottom-water concentrations down to a few meters of sediment depth (i.e., ~70 cmbsf at GE99 29-3, ~180 cmbsf at GE99 24-2, and ~300 cmbsf at GE99 27-2). Below this depth, concentration gradients of the solutes change rapidly, leading to much steeper gradients than observed in the reference cores (Fig. 5). However, early diagenesis at the vent sites is dominated by the same reactions as in the reference cores: anoxic POC degradation and AMO.

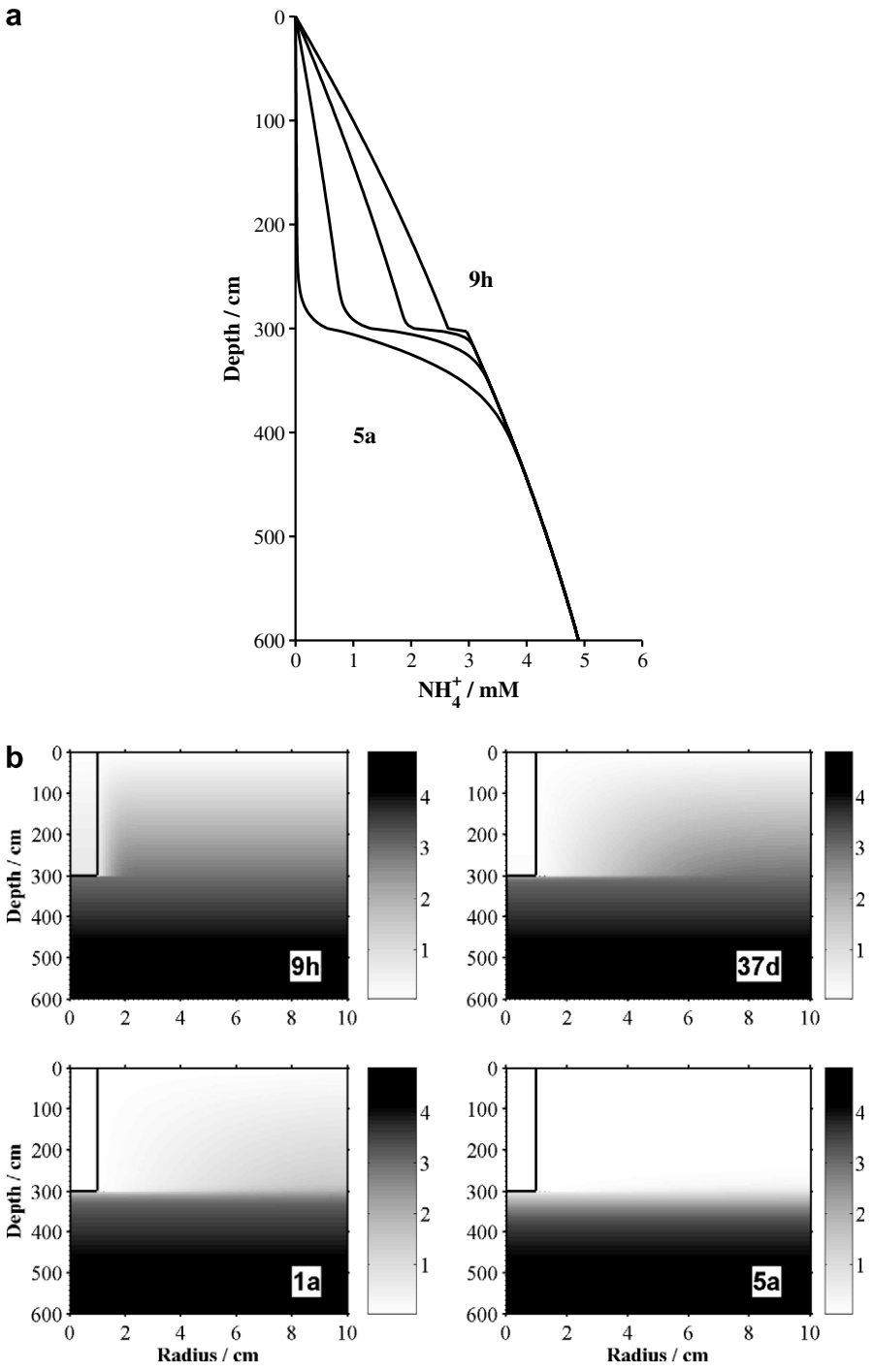

Fig. 6. Time-dependent simulation of the bubble mixing effect on dissolved porewater constituents. NH_4^+ is produced in the sediment with a pseudo zero order reaction rate. Initial condition is the steady state distribution without bubble mixing. Gas bubble mixing occurs only in the upper 3 m of the sediment. (a) Radially averaged 1-D profile of NH_4^+ after 9 h, 37 d, 1 a, and 5 a. (b) Corresponding 3-D NH_4^+ distributions in cylindrical coordinates. An eddy diffusion constant of 1×10^8 cm^2/a, a tube radius of 1 cm (rectangle in the upper left corner), and a tube spacing of 18 cm were chosen for the model simulations shown here.

In a first attempt, Aller's tube model for bioirrigation (Aller, 1980; Boudreau, 1984) has been adopted to describe this phenomena. In a 1-D representation the irrigation of porewater reduces to a simple source/sink term (Eq. (14)). An irrigation constant of at least 0.1 a^{-1} is necessary to reproduce the observed data (dashed lines in Fig. 5). Additionally, in the model simulation a methane concentration of 100 mM at the lower boundary (at 1000 cm) was necessary to account for the higher methane flux from below in order to balance the increased sulphate gradient. Though these cores were recovered from seep sites, the porewater profiles do not indicate upward fluid flow. However, a strongly increased CH_4 flux from below is apparent. Overall, diffusive fluxes are increased by a factor of 3 when compared to those of the background situation. The SO_4^{2-} flux from above totals ~45 μmol/(cm^2 a), ~95% of which is balanced by CH_4 from below. As a consequence, the AMO rate maximum is increased by a factor of 7, from ~300 mM/a at the reference sites to ~2200 mM/a at the vent sites (values are deduced from the 1-D model results). A similar effect of increased AMO rates, as well as a deepening of the reaction front due to bioirrigation, was reported in a modelling study for carbonate crust formation at cold vents (Luff et al., 2004).

Methane gas bubble transport without fluid venting provides the most plausible explanation for the increased methane flux. The emanating gas bubbles lead to numerous intense gas flares observed in the overlying water column by hydro-acoustic methods (Obzhirov et al., 2004). In addition, bioirrigation on the scale of a meter or more is very unlikely, especially in anoxic environments, such as methane vent sites. Organisms that could be responsible for such deep irrigation have never been reported. Therefore, we propose that methane gas bubbles rise through the soft surface sediments, thereby irrigating the porewater and enhancing solute exchange with the overlying bottom-water. Two of the cores, GE99 24-2 and GE99 29-3, recovered the top of a hydrate layer at their base. The formation of surface hydrate layers at cold vents often requires methane supply from gas bubbles (Haeckel et al., 2004), possibly affecting the bubble rise behaviour in the sediment and thus, explaining the shallower mixing depth at these two stations.

4.2. 3-D modelling of the bubble mixing process

The 3-D transport-reaction model for gas bubble mixing consists of 2 primary domains (Fig. 1): the inner bubble tube and the surrounding sediment. During mixing events, eddy diffusion is added to the molecular diffusion (i.e., $K_{eddy} + D_S$) in the bubble tube domain, whereas the effective molecular diffusion, D_S, prevails in the sediment domain. In total, more than 2300 model realizations have been carried out for a wide combination of parameter values (Table 4): 6 different bubble radii, 8 different tube spacings, eddy diffusion coefficients ranging from 10^4 to 10^9 cm^2/a, and simulation times of bubble-induced mixing from 9 h to 50 a.

The effect of gas bubble mixing is demonstrated for porewater ammonium concentrations. This solute is released to the porewater during organic matter decay through a zero-order reaction with respect to ammonium itself and transported by diffusion. Fig. 6 shows an example of the model output for a bubble radius of 1 cm, a tube spacing of 18 cm, and an eddy diffusivity of 10^8 cm^2/a in the tube. This parameter set reproduces the observed NH_4^+ data quite nicely (solid line in Fig. 5) and the bubble radius is a representative average value observed in gassy sediments (Anderson et al., 1998). In the upper panel the radially averaged concentration-depth profile of ammonium for mixing times ranging from 9 h to 5 a is shown, while the respective 3-D distributions are depicted in the lower panel. It takes more than a year of constant bubble ebullition for mixing to change the porewater composition to bottom water values to a sediment depth of 3 m, under the stated conditions. All 3-D model simulations of bubble mixing start from the steady-state model output of the reference station as depicted in Fig. 4 (solid lines) and use a Dirichlet bottom boundary condition of 4.9 mM (see Table 1).

The bottom-water signature is quickly transported to the bottom of the bubble tube. It takes less than 9 h to completely mix the tubewater (Fig. 6, lower panel). Using the well-known Einstein–Smoluchovski relation, $\tau = \frac{\delta^2}{2D}$, the vertical mixing time scale in a bubble tube of a length of $\delta = 300$ cm and a diffusion coefficient of $D = (K_{eddy} + D_S) \approx 10^8$ cm^2/a is assessed to be $\tau = 4$ h. The diffusivity in the sediment domain is about 5 orders of magnitude smaller ($D_{mol}(NH_4^+) = 316$ cm^2/a) and thus, the 3-D concentration profiles clearly show how lateral molecular diffusion slowly transports the ammonium concentration from the surrounding porewater to the tubewater. Finally, after about 5 years a steady state situation is reached with the low bottom-water concentrations down to 300 cmbsf and a subsequent steep increase in NH_4^+ concentrations to about 4 mM at 400 cmbsf (Fig. 6). This model output is equivalent to the one depicted in Fig. 5 (solid lines).

4.3. 3-D parameter sensitivity analysis

A number of parameters, such as horizontal tube spacing, tube radius, mixing time, and bubble rise speed, have been tested for their effects on the bubble-induced porewater mixing process. These model simulations assume the rise of a continuous stream of gas bubbles through the tube, i.e., an eddy diffusion coefficient that is constant over the tube domain and simulation time. In the following sections, we will discuss only selected model results; more figures of the model realizations can be found in the electronic compendium to this article.

4.3.1. Tube spacing and diameter

The horizontal tube spacing was varied from 0.9 to 390 cm with respect to the various tube diameters ranging from 0.1 to 20 cm. Fig. 7a depicts the radially averaged concentrations at 200 cm sediment depth at 5 years into the simulation with a bubble mixing coefficient of 1×10^8 cm^2/a, a tube radius of 1 cm, and various tube spacings. It becomes obvious that mixing is most effective for dense packings of bubble tubes in the sediment, and this efficiency diminishes with increasing distance between the tubes. In addition, there seems to exist a

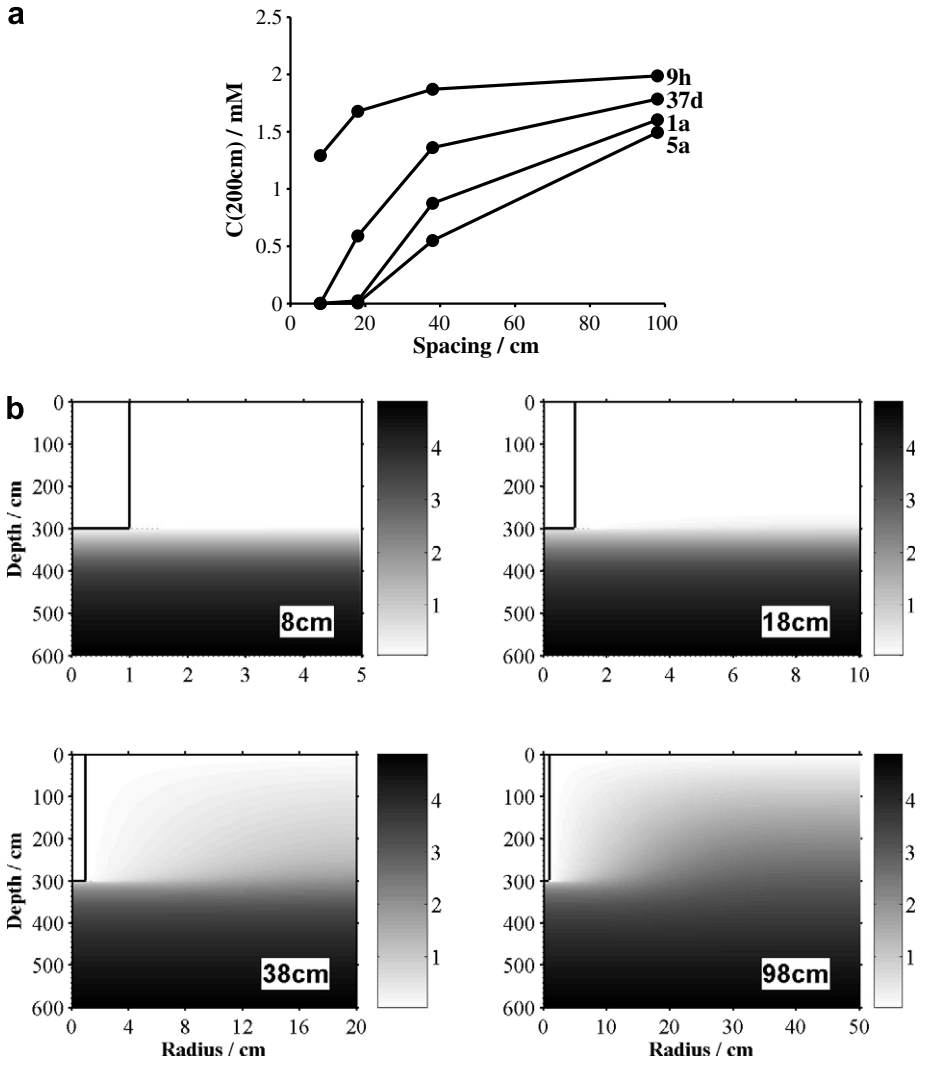

Fig. 7. Effect of horizontal spacing between bubble tubes on mixing efficiency. (a) NH_4^+ concentrations in a sediment depth of 200 cm as a function of the spacing between adjacent tubes at different times of bubble mixing ($t = 9$ h, 37 d, 1 a, and 5 a). Dots represent results of model realizations. (b) Corresponding 3-D NH_4^+ distributions after a mixing time of 5 years for tube spacings of 8, 18, 38, and 98 cm, respectively. Note the different scales for the x-axis. An eddy diffusion constant of 1×10^8 cm^2/a and a tube radius of 1 cm (rectangle in the upper left corner) were chosen for these model realizations.

maximum spacing, above which bottom-water concentrations can no longer be mixed into depth. In this example, the critical tube spacing is somewhere above 40 cm. Fig. 7b presents the respective 2D ammonium distribution in the model domains after 5 years for tube spacings of 8, 18, 38, and 98 cm. While mixing within the bubble tube itself is very effective, vertical diffusion starts to dominate over lateral diffusion with increasing distance from the tube. As a result, downward mixing of bottom-water into the sediment is incomplete for a tube spacing of 98 cm.

In contrast, the tube diameter has a less dominant effect on the efficiency of the mixing process (see Electronic supplement for additional figures). However, for very narrow tubes flushing of the tube with bottom-water becomes very difficult because lateral solute transport quickly levels out the concentration difference between bubble tube and sediment. Thus, for narrow tube diameters and small tube spacings almost no radial concentration gradients can occur within the sediment, but only a vertical gradient develops over the simulation time. In addition, mixing of bottom-water concentrations into the sediment remains incomplete for tube spacings above 10 cm.

4.3.2. Time-dependent irrigation

The effect of bubble mixing was simulated for a total time of up to 50 years. In most cases a steady state situation was reached much earlier. Fig. 8 illustrates the changes of the radially averaged NH_4^+ concentration with time at a sediment depth of 200 cm for a variety of eddy diffusivities and thus, also allows estimation of the time to reach steady state for the respective parameter combinations. In the upper panel (a) the tube spacing was chosen to be 18 cm, and in the lower panel (b) it was 98 cm. The radially averaged NH_4^+ concentration at 200 cmbsf slowly decreases

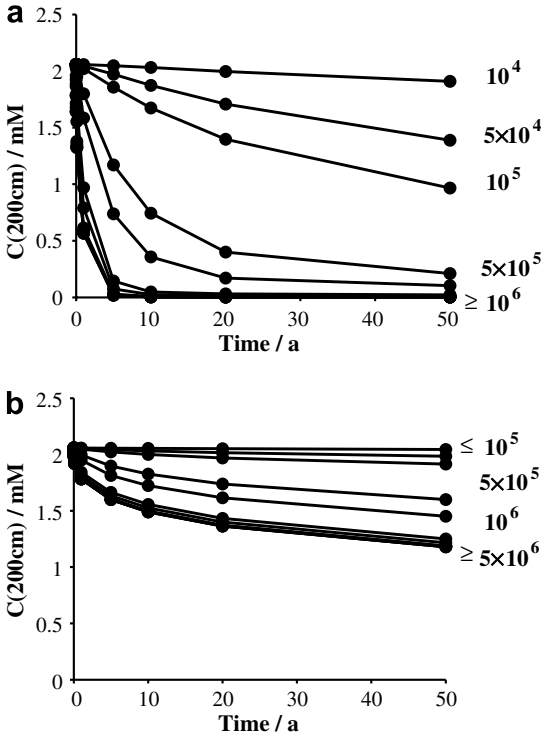

Fig. 8. NH_4^+ concentrations at a sediment depth of 200 cm are plotted as a function of the mixing time for eddy diffusivities between 10^4 and 10^9 cm^2/a. Dots represent results of model realizations for (a) a tube spacing of 18 cm and (b) 98 cm. The tube radius is 1 cm in all depicted model realizations.

while the mixing proceeds. Again, the dependence of the mixing efficiency on the tube spacing becomes apparent when comparing Fig. 8a and b: even high eddy diffusivities ($>5\times10^6$ cm^2/a) do not allow for sufficient mixing of bottom-water NH_4^+ concentrations (i.e., 0 mM) to 200 cmbsf if the spacing is large (lower panel, b). Conversely, for a high density of bubble tubes (upper panel, a), the mixing can reach bottom-water concentrations within a few years.

While it generally takes between a few years and 1 or 2 decades of gas bubble ebullition to produce a fully irrigated concentration profile, this porewater distribution is quite stable after the gas flow has ceased (Fig. 9). The model simulation started with the well-mixed ammonium profile shown in Fig. 6 as initial condition and considered NH_4^+ release due to organic matter degradation and molecular diffusion in the sediment domain, as well as molecular diffusion in the tube domain, but no bubble-induced mixing. A bubble radius of 1 cm and a dense tube distribution with a spacing of 18 cm were chosen for these depicted results. Since molecular diffusion is orders of magnitude slower than the bubble-induced eddy diffusion, the well-mixed initial profile is maintained for several years (Fig. 9b). In total, it takes more than 500 years to return to the "normal" background NH_4^+ distribution characterizing the 'no-vent' situation (Fig. 9a).

4.3.3. Eddy diffusivity

Eddy diffusivities were varied over 5 orders of magnitude (10^4–10^9 cm^2/a). As expected, the efficiency of bubble-induced irrigation increases with increasing diffusivity (Fig. 8). This effect is even more obvious for simulations with low tube spacing (e.g., 18 cm in Fig. 8a). Low eddy diffusivities, i.e., up to two orders of magnitude above the molecular diffusion coefficient, are insufficient to create bottom-water concentration conditions at 200 cmbsf. For large tube spacing, mixing efficiency increases with time, but remains incomplete even at very high eddy diffusivities (Fig. 8b). Overall, the model realizations (see also additional graphs in the Electronic supplement) reveal that there seems to be a threshold eddy coefficient of generally 5×10^6 cm^2/a, above which the mixing efficiency is enhanced.

Additionally, the relative competition between the bubble-induced porewater mixing and the production (or consumption) of solutes can be deduced. In our example, ammonium is produced with a moderate to slow rate of organic matter degradation ($k_G < 10^{-4}$ a^{-1}) and thus, at high K_{eddy} values, bubble mixing is the dominant process. In contrast, at low eddy diffusivities, the production of ammonium becomes dominant. From this we can also infer that faster diagenetic reactions will require higher eddy diffusivities in order to sustain the irrigation pattern for porewater constituents. Again, the Einstein–Smoluchovski relation is a suitable assessment tool: bubble-induced irrigation is the dominant process as long as its time scale is shorter than of any reaction. While the time scale of a K_{eddy} value of 10^8 cm^2/a was ~4 h, a low value of $K_{eddy} = 10^4$ cm^2/a has a time scale of ~4.5 a and hence, even slow organic matter degradation becomes important.

4.4. Ebullition of bubble pulses

In Section 4.2 and 4.3, the model realizations involved eddy diffusion coefficients representing continuous streams of gas bubbles rising in the tubes. However, in natural settings, such as cold seeps and methanogenic surface sediments, pulses of methane gas ebullition alternating with intermittent intervals of quiescence are more commonly observed. Hence, bubble pulses were simulated by applying a Gaussian function to the distribution of the eddy diffusivity over the tube length and simulation time (Eq. (18); Fig. 1b). The Gaussian distribution was chosen for numerical stability reasons to provide a smooth transition between the situation of gas bubble mixing and purely molecular diffusion in the tube domain. Nevertheless, these model simulations turned out to be computationally expensive: a 'pulsed' model run took ~3 months (simulating 0.2 a) on a 2 GHz CPU, compared to only minutes to hours for a simulation of a continuous bubble stream (simulating the total of 50 a). When simulating bubble pulses, the automated PDE solver takes only very small time-steps in the order of milliseconds, whereas for constant K_{eddy} values this time-step can increase rapidly (to days and weeks) during simulations, and numerical stability is still maintained.

Fig. 10 shows the model results of pulsed bubble ebullition (dots), i.e. the difference between the initial NH_4^+ concentration ($C_0 = 2$ mM) at 200 cmbsf and the actual concentration (C_t) as a function of time. The bubble pulse has a half-height peak width of ~5 cm, which is equivalent

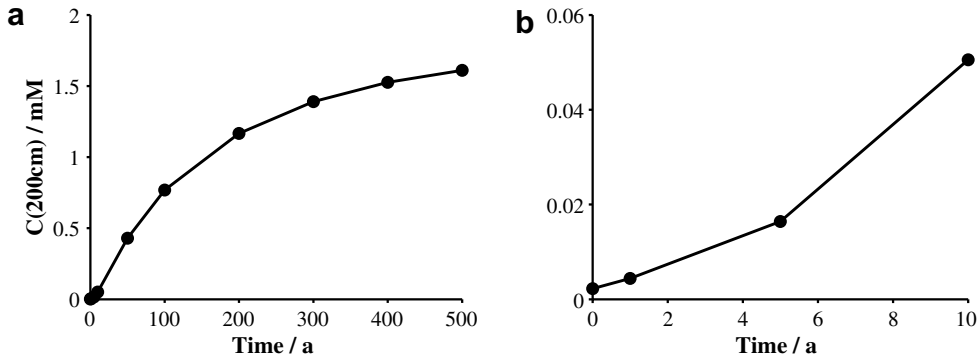

Fig. 9. Evolution of NH_4^+ concentration at a sediment depth of 200 cm with time after bubble mixing has ceased. Right panel is a blow-up of the left plot for $t = 0$–10 a. Initial condition is the well-mixed profile of Fig. 6. Model geometries are a bubble radius of 1 cm and a tube spacing of 18 cm.

to 2–3 gas bubbles of radius $r_1 = 1$ cm ascending through the tube at all times. The corresponding parameters in Eq. (17) are: $\sigma = 3.16$ cm and $K_0 = 1 \times 10^8$ cm^2/a. The outer wall tube spacing, $2(r_2 - r_1)$, is 18 cm. For comparison, the model results of continuous bubble streams and identical tube geometries are plotted for a range of K_{eddy} values (solid lines). Thus, a pulse of ~2 gas bubbles with an eddy diffusivity of 1×10^8 cm^2/a is equivalent to a continuous bubble stream with an eddy diffusion coefficient of $\sim 2 \times 10^6$ cm^2/a. This value is equal to the mean value of the K_{eddy} distribution over the tube length and simulation time (Eq. (19)).

Hence, the mean eddy diffusivity, $\langle K_{eddy} \rangle$, decreases quickly as the time interval of quiescence (i.e., no bubble ebullition) increases (Fig. 11a). In the same way, $\langle K_{eddy} \rangle$ increases as the bubble pulses become longer (Fig. 11b). The theoretical maximum number of bubbles in the tube is, of course, given by the bubble radius. Hence, in a tube with a length of 300 cm, 150 bubbles with a radius of 1 cm will lead to a continuous stream of bubbles with no quiescent periods.

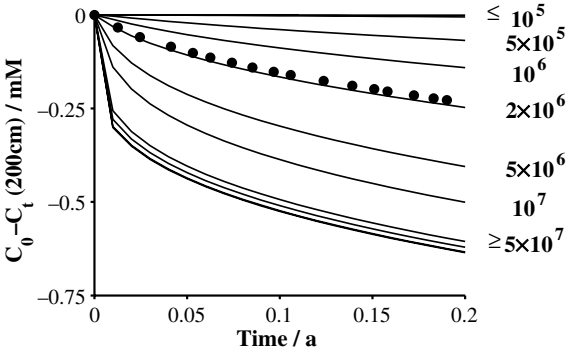

Fig. 10. Porewater mixing of a pulsed bubble flux (dots) versus continuous bubble streams (lines) of various eddy diffusivities. The change of NH_4^+ concentration with time at a sediment depth of 200 cm is depicted for a tube radius of 1 cm and a tube spacing of 18 cm. The bubble pulse has a maximum eddy diffusivity of $K_{eddy} = 1 \times 10^8$ cm^2/a.

Finally, we can translate $\langle K_{eddy} \rangle$ values into bubble frequencies (Eq. (20); Fig. 2b) and a gas flow (Eq. (21)). Within our assumption for the 3-D model geometry of spherical bubbles, gas bubbles with a radius of 1 cm rising at a speed of 1.6 cm/s (i.e., $K_{eddy} \approx 1 \times 10^8$ cm^2/a) carry a methane volume flux of $\sim 4 \times 10^5$ L/(m^2 a) (i.e., Eq. (21)), if there are 4 bubble tubes per m^2 (i.e., a tube spacing of ~40 cm). Under the in situ conditions of the Obzhirov Flare area ($p = 70$ atm, $T = 2.4$ °C), this volume flux results in a methane flux of $\sim 1 \times 10^6$ mol/(m^2 a). A rise velocity of ~0.2 mm/s (i.e., $K_{eddy} \approx 1 \times 10^6$ cm^2/a) would result in a CH_4 flux that is 2 orders of magnitude smaller, i.e., $F_{CH_4} = 4 \times 10^3$ L/(m^2 a) (i.e., $\sim 1 \times 10^4$ mol/(m^2 a)). Overall, the simulated methane fluxes range from 5×10^1 to 1×10^9 L/(m^2 a) with a minimum CH_4 flux necessary to achieve a visual mixing effect within several weeks or months of 1×10^3–1×10^5 L/(m^2 a). Since gas bubbles in sediments may, in fact, be hindered by interaction with the sediment (i.e., friction), these methane fluxes may be overestimated. In addition, the shape of the bubbles may not be spherical (Boudreau et al., 2005). A volume of 0.3 cm^3 was reported for a disc-shaped bubble of 2 cm size (Boudreau et al., 2005), as compared to a volume of 4.2 cm^3 for a truly spherical bubble with the same diameter of 2 cm.

4.5. Linking 1-D and 3-D bubble-induced irrigation

The 1-D expression for porewater irrigation (Eq. (14)) assumes that mixing occurs on a much faster time scale than solutes are transported by molecular diffusion and advection. Thus, the water in the tube is 'instantaneously' flushed with bottom-water. Similar predictions are made by the 3-D model realizations: generally, the bubble tube was well-flushed within hours or days, if a minimum K_{eddy} of 5×10^5–5×10^6 cm^2/a was applied. The larger the tube (i.e., the bubble), the easier the tubewater is mixed. Only for tube radii <0.1 cm were larger eddy diffusivities of 1×10^8 cm^2/a necessary to create quickly bottom-water values in the tube. In the latter case, lateral diffusion becomes dominant, because the tube domain is so small. Thus, the minimum eddy diffusivity necessary to keep the tube well-flushed is equivalent to a CH_4 flux per bubble tube of

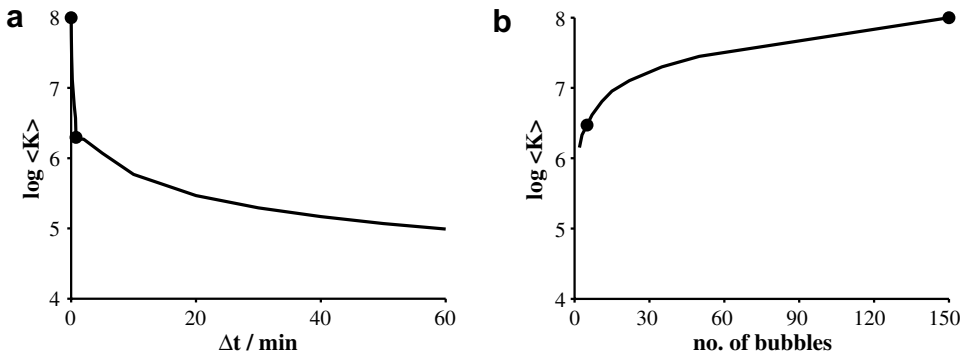

Fig. 11. Spatially and temporally averaged eddy diffusivity of bubble pulses based on Eqs. (18) and (19) with a K_{eddy} of 1×10^8 cm/a. (a) As a function of time between pulses and (b) as a function of spatial distance between pulses in tube (i.e., number of bubbles in the tube at all times). The bubble pulse has a half-height peak width of ~5 cm, the tube radius is 1 cm and the spacing between tubes is 18 cm. The dots represent the results of the pulsed model realization (i.e., $\log\langle K\rangle = 6.3$; see also Fig. 10) and a continuous bubble stream (i.e., $\log\langle K\rangle = 8$).

5×10^2–5×10^3 L/a, provided the average bubble radius is 1 cm (Eq. (21)).

For a given tube radius, the irrigation coefficient itself implies a certain tube density per unit area (Eq. (15)). For example, an irrigation coefficient of $\alpha = 0.1\ a^{-1}$, i.e., the result of the 1-D model simulation in Section 4.1.2, and our assumed tube radius of $r_1 = 1$ cm require the radius of the sediment domain, r_2, to be >17.5 cm, i.e., a tube spacing >33 cm. Similarly, a tube geometry of $r_1 = 1$ cm and $r_2 = 10$ cm, i.e., a tube spacing of 18 cm, defines the irrigation coefficient to be $\alpha > 0.57\ a^{-1}$. Thus, the resulting spatial methane fluxes based on these irrigation coefficients are 5×10^3–5×10^4 L/(m^2 a) and 2×10^4–2×10^5 L/(m^2 a), respectively.

Additionally, if the tube spacing, $2(r_2 - r_1)$, becomes large (i.e., $r_2 \to \infty$ in Eq. (15)), the 1-D irrigation coefficient tends towards zero (i.e., $\alpha \to 0$) and the mixing becomes ineffective. This resembles a similar result obtained with the 3-D mixing model (see Figs. 7 and 8).

The major drawback of the 1-D representation of porewater irrigation is that fitting the model to the data will always yield only a minimum irrigation coefficient, which might not be defined for the actual tube geometry. In turn, the actual tube geometry will require much higher irrigation coefficients than can be determined by any fitting procedure. Thus, the methane flux calculated from irrigation coefficients might be quite flawed because the radial transport information is not well represented in the 1-D source/sink term.

5. CONCLUSIONS

Our 3-D modelling study shows that gas bubble-induced irrigation of porewater can mix bottom-water concentrations into the sediment on meter scales. General requirements for the observation of such porewater profiles are: (1) gas bubble rise velocities corresponding to a $K_{eddy} \geqslant 1 \times 10^5$ cm^2/a, (2) a density of at least 4 tubes/m^2 (i.e., a distance of 40 cm between bubble tubes), (3) active gas seepage for at least a few weeks or months, and (4) moderate to low diagenetic reaction rates of solutes.

Thus, bubble irrigation with a visual effect similar to that observed in cores from vent sites northeast off Sakhalin Island, Sea of Okhotsk, is predicted by the 3-D model to create CH_4 fluxes of 1×10^3–5×10^5 L/(m^2 a) (i.e., 3×10^3–1×10^6 mol/(m^2 a)), lasting for, at least, a few weeks to months. The resulting porewater profiles are stable for several years to decades without further gas bubble ebullition. Our estimated CH_4 fluxes lie well within the range of methane fluxes reported from other areas with active methane seepage. One example, given here for comparison is the well-studied Hydrate Ridge, Cascadia margin with (a) 1×10^3–1×10^4 mol/(m^2 a) for methane hydrate formation (Haeckel et al., 2004) and (b) 4×10^5 mol/(m^2 a) for discrete discharge at Hydrate Ridge (Torres et al., 2002), and (c) an average of 24 mol/(m^2 a) over the entire area of 4×10^5 m^2 (Torres et al., 2004). The second example is the Coal Oil Point gas seep with 8×10^7 mol/(m^2 a) (Boles et al., 2001).

Besides, providing a handle on quantifying methane gas transport and fluxes in sediments, our model simulations also show that gas bubble transport in surface sediments significantly enhances solute transport by means of eddy diffusion. Several studies have reported increased diffusivities of solutes in gassy sediments, such as coastal areas, lakes, and wetlands, but could not provide satisfactory explanations. For example, Martens and Berner (1974), Martens (1976), Martens et al. (1980) showed that in the anoxic sediments of Cape Lookout Bight, North Carolina, solute diffusivities are 2–3 times higher than molecular diffusion. They could, of course, not observe any visual mixing effect because the eddy diffusivities are too small, but the process is still important for solute exchange with the overlying water, as numerical analysis has proved. Similar observations were made by e.g., Rothfuss and Conrad (1998) in the upper layers of an anoxic paddy soil and Strayer and Tiedje (1978) for lake sediments. Additionally, Brennwald et al. (2005) observed an unusual isotopic signature of dissolved gases that is most likely caused by eddy diffusion, rather than molecular diffusion. Whereas molecular diffusion affects the isotopic composition, eddy diffusion would not because it is a macroscopic physical process and as such does not lead to isotope fractionation, i.e., all isotopes are mixed equally.

Eddy diffusion associated with bubble rise can be orders of magnitudes larger than molecular diffusion and hence plays an important role in transporting solutes in anoxic sediments, where methane is released by bubble ebullition into the overlying water column (and atmosphere), e.g. wetlands, high productivity coastal sediments, hydrate bearing surface sediments. This irrigation process increases diffusive solute fluxes and thus leads to enhanced biogeochemical turnovers.

ACKNOWLEDGMENTS

The authors would like to thank B. Domeyer, R. Surberg, and A. Bleyer for sample processing and measurements. We would also like to acknowledge critical comments from F. Meysman, P. Jewell, and an anonymous third reviewer that substantially improved this manuscript. The work was supported by the German Federal Ministry of Education and Research, project grants KOMEX II (No. 03G0568A), SO178-KOMEX, and COMET (No. 03G0600D). M. Haeckel was supported by the Alexander von Humboldt Foundation, Bonn. Additional support was provided by US ONR.

APPENDIX A. SUPPLEMENTARY DATA

The electronic annex contains additional figures for the 3-D parameter sensitivity analysis regarding tube spacing, tube radius, mixing time, and eddy diffusivity (corresponding to Figs. 6–8 in the article). Supplementary data associated with this article can be found, in the online version, at doi:10.1016/j.gca.2007.08.011.

REFERENCES

Aller R. C. (1980) Quantifying solute distributions in the bioturbated zone of marine sediments by defining an average microenvironment. *Geochim. Cosmochim. Acta* **44**, 1955–1965.

Aller R. C. and Aller J. Y. (1992) Meiofauna and solute transport in marine muds. *Limnol. Oceanogr.* **37**, 1018–1033.

Anderson A. L., Abegg F., Hawkins J. A., Duncan M. E. and Lyons A. P. (1998) Bubble populations and acoustic interaction with the gassy floor of Eckernförde Bay. *Cont. Shelf Res.* **18**, 1807–1838.

Antoine D., André J. M. and Morel A. (1996) Oceanic primary production: 2. Estimation at global scale from satellite (coastal zone color scanner) chlorophyll. *Global Biogeochem. Cycles* **10**, 57–69.

Berner R. A. (1980) *Early Diagenesis—A Theoretical Approach*. Princeton University Press, Princeton, NJ.

Biebow, N. and Hütten, E. (1999) Cruise Report KOMEX I and KOMEX II: RV Professor Gargarinsky cruise 22, RV Akademik M.A. Lavrentyev cruise 28. GEOMAR, Kiel.

Biebow, N., Lüdmann, T., Karp, B. and Kulinich, R. (2000) Cruise Report KOMEX V and KOMEX VI: RV Professor Gargarinsky cruise 26, MV Marshal Gelovany cruise 1. GEOMAR, Kiel.

Boles J. R., Clark J. F., Leifer I. and Washburn L. (2001) Temporal variation in natural methane seep rate due to tides, Coal Oil Point area, California. *J. Geophys. Res.* **106**, 27077–27086.

Boudreau B. P. (1984) On the equivalence of nonlocal and radial-diffusion models for porewater irrigation. *J. Mar. Res.* **42**, 731–735.

Boudreau B. P. (1987) A steady-state diagenetic model for dissolved carbonate species and pH in the porewaters of oxic and suboxic sediments. *Geochim. Cosmochim. Acta* **51**, 1985–1996.

Boudreau B. P. (1996) A method-of-lines code for carbon and nutrient diagenesis in aquatic sediments. *Comput. Geosci.* **22**, 479–496.

Boudreau B. P. (1997) *Diagenetic Models and their Implementation: Modelling Transport and Reactions in Aquatic Sediments*. Springer, Berlin, Heidelberg, NY.

Boudreau B. P., Algar C., Johnson B. D., Croudace I., Reed A., Furukawa Y., Dorgan K. M., Jumars P. A., Grader A. S. and Gardiner B. S. (2005) Bubble growth and rise in soft sediments. *Geology* **33**, 517–520.

Boudreau B. P. and Canfield D. E. (1988) A provisional diagenetic model for pH in anoxic porewaters: application to the FOAM site. *J. Mar. Res.* **46**, 429–455.

Brennwald M. S., Kipfer R. and Imboden D. M. (2005) Release of gas bubbles from lake sediment traced by noble gas isotopes in the sediment pore water. *Earth Planet. Sci. Lett.* **235**, 31–44.

Brown P. N., Byrne G. D. and Hindmarsh A. C. (1989) VODE: a variable-coefficient ODE solver. *SIAM J. Sci. Stat. Comput.* **10**, 1038–1051.

Chanton J. P., Martens C. S. and Kelley C. A. (1989) Gas transport from methane-saturated, tidal freshwater and wetland sediments. *Limnol. Oceanograph.* **34**, 807–819.

Clegg S. L. and Whitfield M. (1995) A chemical model of seawater including dissolved ammonia and the stoichiometric dissociation constant of ammonia in estuarine water and seawater from −2 to 40 °C. *Geochim. Cosmochim. Acta* **59**, 2403–2421.

Davies R. M. and Taylor G. (1950) The mechanics of large bubbles rising through extended liquids and through liquids in tubes. *Proc. R. Soc. Lond. A* **200**, 375–390.

Dimitrov L. I. (2002) Mud volcanoes—the most important pathway for degassing deeply buried sediments. *Earth Sci. Rev.* **59**, 49–76.

Dimitrov L. I. (2003) Mud volcanoes—a significant source of atmospheric methane. *Geo-Mar. Lett.* **23**, 155–161.

Fossing H., Ferdelman T. G. and Berg P. (2000) Sulfate reduction and methane oxidation in continental margin sediments influenced by irrigation (South-East Atlantic off Namibia). *Geochim. Cosmochim. Acta* **64**, 897–910.

Gardiner B. S., Boudreau B. P. and Johnson B. D. (2003) Growth of disk-shaped bubbles in sediments. *Geochim. Cosmochim. Acta* **67**, 1485–1494.

Ginsburg G. D., Soloviev V. A., Cranston R. E., Lorenson T. D. and Kvenvolden K. A. (1993) Gas hydrates from the continental slope, offshore Sakhalin Island, Okhotsk Sea. *Geo-Mar. Lett.* **13**, 41–48.

Grasshoff K., Ehrhardt M. and Kremling K. (1999) *Methods of Seawater Analysis*. Wiley-VCH, Weinheim.

Grigg N. J., Boudreau B. P., Webster I. T. and Ford P. W. (2005) The nonlocal model of porewater irrigation: limits to its equivalence with a cylinder diffusion model. *J. Mar. Res.* **63**, 437–455.

Haeckel M., König I., Riech V., Weber M. and Suess E. (2001) Pore water profiles and numerical modelling of Peru Basin deep-sea sediments. *Deep-Sea Res. II* **48**, 3713–3736.

Haeckel M., Suess E., Wallmann K. and Rickert D. (2004) Rising methane gas-bubbles form massive hydrate layers at the seafloor. *Geochim. Cosmochim. Acta* **68**, 4335–4345.

IPCC (2001). Climate Change 2001: The Scientific Basis. Contribution of Working Group I to the Third Assessment Report of the Intergovernmental Panel on Climate Change. Cambridge Univerity Press, Cambridge, UK.

Johnson B. D., Boudreau B. P., Gardiner B. S. and Maas R. (2002) Mechanical response of sediments to bubble growth. *Mar. Geol.* **187**, 347–363.

Jørgensen B. B., Weber A. and Zopfi J. (2001) Sulfate reduction and anaerobic methane oxidation in Black Sea sediments. *Deep-Sea Res. I* **48**, 2097–2120.

Judd A. G. (2003) The global importance and context of methane escape from the seabed. *Geo-Mar. Lett.* **23**, 147–154.

Judd A. G., Hovland M., Dimitrov L. I., Garcia-Gil S. and Jukes V. (2002) The geological methane budget at continental margins and its influence on climate change. *Geofluids* **2**, 109–126.

Kipphut G. W. and Martens C. S. (1982) Biogeochemical cycling in an organic-rich coastal marine basin III. Dissolved gas transport in methane-saturated sediments. *Geochim. Cosmochim. Acta* **46**, 2049–2060.

Leifer I., Boles J. R., Luyendyk B. P. and Clark J. F. (2004) Transient discharges from marine hydrocarbon seeps: spatial and temporal variability. *Environ. Geol.* **46**, 1038–1052.

Li Y.-H. and Gregory S. (1974) Diffusion of ions in sea water and in deep-sea sediments. *Geochim. Cosmochim. Acta* **38**, 703–714.

Lüdmann T. and Wong K. K. (2003) Characteristics of gas hydrate occurences associated with mud diapirism and gas escape structures in the northwestern Sea of Okhotsk. *Mar. Geol.* **201**, 269–286.

Luff R., Haeckel M. and Wallmann K. (2001) Robust and fast FORTRAN and MATLAB libraries to calculate pH distributions in a non-steady state model for aqueous systems. *Comput. Geosci.* **27**, 157–169.

Luff R., Wallmann K. and Aloisi G. (2004) Numerical modeling of carbonate crust formation at cold vent sites: Significance for fluid and methane budgets and chemosynthetic biological communities. *Earth Planet. Sci. Lett.* **221**, 337–353.

MacDonald I. R., Leifer I., Sassen R., Stine P., Mitchell R. and Guinasso J. R. (2002) Transfer of hydrocarbons from natural seeps to the water column and atmosphere. *Geofluids* **2**, 95–107.

Martens C. S. (1976) Control of methane sediment-water bubble transport by macroinfaunal irrigation in Cape Lookout Bight, North Carolina. *Science* **192**, 998–1000.

Martens C. S., Albert D. B. and Alperin M. J. (1998) Biogeochemical processes controlling methane in gassy coastal sediments—Part 1. A model coupling organic matter flux to gas production, oxidation and transport. *Cont. Shelf Res.* **18**, 1741–1770.

Martens C. S. and Berner R. A. (1974) Methane production in interstitial waters of sulfate-depleted marine sediments. *Science* **185**, 1167–1169.

Martens C. S., Kipphut G. W. and Klump J. V. (1980) Sediment-water chemical exchange in the coastal zone traced by in situ Radon-222 flux measurements. *Science* **208**, 285–288.

Martens C. S. and Klump J. V. (1980) Biogeochemical cycling in an organic-rich coastal marine basin I. Methane sediment-water exchange processes. *Geochim. Cosmochim. Acta* **44**, 471–490.

Martin W. R., Bender M., Leinen M. and Orchardo J. (1991) Benthic organic carbon degradation and biogenic silica dissolution in the central equatorial Pacific. *Deep-Sea Res.* **38**, 1481–1516.

Matveeva T., Soloviev V., Wallmann K., Obzhirov A., Biebow N., Poort J., Salomatin A. and Shoji H. (2003) Geochemistry of gas hydrate accumulation offshore NE Sakhalin Island (the Sea of Okhotsk): results from the KOMEX-2002 cruise. *Geo-Mar. Lett.* **23**, 278–288.

McGinnis D., Greinert J., Artemov Y., Beaubien S. E. and Wüest A. (2006) Fate of rising methane bubbles in stratified waters: how much methane reaches the atmosphere? *J. Geophys. Res.* **111**. doi:10.1029/2005JC003183.

Meile C., Berg P., Van Cappellen P. and Tuncay K. (2005) Solute-specific pore water irrigation: implications for chemical cycling in early diagenesis. *J. Mar. Res.* **63**, 601–621.

Meile C., Koretsky C. M. and Van Cappellen P. (2001) Quantifying bioirrigation in aquatic sediments: an inverse modeling approach. *Limnol. Oceanogr.* **46**, 164–177.

Melgaard D. K. and Sincovec R. F. (1981a) ALGORITHM 565: PDETWO/PSETM/GEARB: solution of systems of two-dimensional nonlinear partial differential equations. *ACM Trans. Math. Softw.* **7**, 126–135.

Melgaard D. K. and Sincovec R. F. (1981b) General software for two-dimensional nonlinear partial differential equations. *ACM Trans. Math. Softw.* **7**, 106–125.

Milkov A. V. and Etiope G. (2005) Global methane emission through mud volcanoes and its past and present impact on the Earth's climate—a comment. *Int. J. Earth Sci.* **94**, 490–492.

Milkov A. V., Sassen R., Apanasovich T. V. and Dadashev F. G. (2003) Global gas flux from mud volcanoes: a significant source of fossil methane in the atmosphere and the ocean. *Geophys. Res. Lett.* **30**, 1037. doi:10.1029/2002GL016358.

Millero F. J. (1983) Influence of pressure on chemical processes in the sea. In *Chemical Oceanography* (eds. J. P. Riley and R. Chester). Academic Press.

Millero F. J. (1995) Thermodynamics of the carbon dioxode system in the oceans. *Geochim. Cosmochim. Acta* **59**, 661–677.

Murray J. W., Grundmanis V. and Smethie W. M. (1978) Interstitial water chemistry in the sediments of Saanich Inlet. *Geochim. Cosmochim. Acta* **42**, 1011–1026.

Niewöhner C., Hensen C., Kasten S., Zabel M. and Schulz H. D. (1998) Deep sulfate reduction completely mediated by anaerobic methane oxidation in sediments of the upwelling area off Namibia. *Geochim. Cosmochim. Acta* **62**, 455–464.

Nürnberg D. and Tiedemann R. (2004) Environmental change in the Sea of Okhotsk during the last 1.1 million years. *Paleoceanography* **19**. doi:10.1029/2004PA001023.

Obzhirov A., Shakirov R., Salyuk A., Suess E., Biebow N. and Salomatin A. (2004) Relations between methane venting, geological structure and seismo-tectonics in the Okhotsk Sea. *Geo-Mar. Lett.* **24**, 135–139.

Prandtl L. and Tietjens O. G. (1957) *Fundamentals of Hydro- and Aerodynamics*. Dover Publications Inc..

Press W. H., Teukolsky S. A., Vetterling W. T. and Flannery B. P. (1992) *Numerical Recipes in FORTRAN 77: The Art of Scientific Computing*. Cambridge University Press, Cambridge.

Rabouille C. and Gaillard J.-F. (1991a) A coupled model representing the deep-sea organic carbon mineralization and oxygen consumption of surficial sediments. *J. Geophys. Res.* **96**, 2761–2776.

Rabouille C. and Gaillard J.-F. (1991b) Towards the EDGE: Early diagenetic global explanation. A model depicting the early diagenesis of organic matter, O_2, NO_3, Mn, and PO_4. *Geochim. Cosmochim. Acta* **55**, 2511–2525.

Reeburgh W. S. (1969) Observations of gases in Chesapeake Bay sediments. *Limnol. Oceanogr.* **14**, 368–375.

Rothfuss F. and Conrad R. (1998) Effect of gas bubbles on the diffusive flux of methane in anoxic paddy soil. *Limnol. Oceanogr.* **434**, 1511–1518.

Sauter E., Muyakshin S. I., Charlou J.-L., Schlüter M., Boetius A., Jerosch K., Damm E., Foucher J.-F. and Klages M. (2006) Methane discharge from a deep-sea submarine mud volcano into the upper water column by gas hydrate-coated methane bubbles. *Earth Planet. Sci. Lett.* **243**, 354–365.

Schlüter M., Sauter W., Hansen H.-P. and Suess E. (2000) Seasonal variations of bioirrigation in coastal sediments: modelling of field data. *Geochim. Cosmochim. Acta* **64**, 821–834.

Schulz H. D., Dahmke A., Schinzel U., Wallmann K. and Zabel M. (1994) Early diagenetic processes, fluxes, and reaction rates in sediments of the South Atlantic. *Geochim. Cosmochim. Acta* **58**, 2041–2060.

Shakirov R., Obzhirov A., Suess E., Salyuk A. and Biebow N. (2004) Mud volcanoes and gas vents in the Okhotsk Sea area. *Geo-Mar. Lett.* **24**, 140–149.

Strayer R. F. and Tiedje J. M. (1978) In situ methane production in a small, hypereutrophic, hard-water lake: Loss of methane from sediments by vertical diffusion and ebullition. *Limnol. Oceanogr.* **23**, 1201–1206.

Tishchenko P., Hensen C., Wallmann K. and Wong C. S. (2005) Calculation of the stability and solubility of methane hydrate in seawater. *Chem. Geol.* **219**, 37–52.

Torres M. E., McManus J., Hammond D. E., de Angelis M. A., Heeschen K. U., Colbert S. L., Tryon M. D., Brown K. M. and Suess E. (2002) Fluid and chemical fluxes in and out of sediments hosting methane hydrate deposits on Hydrate Ridge, OR, I: Hydrological provinces. *Earth Planet. Sci. Lett.* **201**, 525–540.

Torres M. E., Wallmann K., Trehu A. M., Bohrmann G., Borowski W. S. and Tomaru H. (2004) Gas hydrate growth, methane transport, and chloride enrichment at the southern summit of Hydrate Ridge, Cacadia margin off Oregon. *Earth Planet. Sci. Lett.* **226**, 225–241.

Van Cappellen P. and Gaillard J.-F. (1996) Biogeochemical dynamics in aquatic sediments. In *Reactive Transport in Porous Media* (eds. P. C. Lichtner, C. I. Steefel and E. H. Oelkers). Mineralogical Society of America, Washington, DC, pp. 335–376.

Van Cappellen P., Gaillard J.-F. and Rabouille C. (1993) Biogeochemical transformations in sediments: kinetic models of early diagenesis. In *Interactions of C, N, P and S. Biogeochemical Cycles and Global Change* (eds. R. Wollast, F. T. Mackenzie and L. Chou). Springer, Berlin, Heidelberg, pp. 401–445.

Van Cappellen P. and Wang Y. (1996) Cycling of iron and manganese in surface sediments: general theory for the coupled transport and reaction of carbon, oxygen, nitrogen, sulfur, iron, and manganese. *Am. J. Sci.* **296**, 197–243.

Wallmann K., Aloisi G., Haeckel M., Obzhirov A. and Tishchenko P. (2006a) Kinetics of organic matter degradation, microbial methane generation, and gas hydrate formation in anoxic marine sediments. *Geochim. Cosmochim. Acta* **70**, 3905–3927.

Wallmann K., Drews M., Aloisi G. and Bohrmann G. (2006b) Methane discharge into the Black Sea and the global ocean via fluid flow through submarine mud volcanoes. *Earth Planet. Sci. Lett.* **248**, 544–559.

Wong H. K., Lüdmann T., Baranov B. V., Karp B. Y., Konerding P. and Ion G. (2003) Bottom current-controlled sedimentation and mass wasting in the northwestern Sea of Okhotsk. *Mar. Geol.* **201**, 287–305.

Associate editor: Robert C. Aller